A potential post-perovskite province in D″ beneath the Eastern Pacific: Evidence from new analysis of discrepant SKS-SKKS shear-wave splitting

Joseph Asplet[1], James Wookey[1] & Michael Kendall[1]

[1]School of Earth Sciences, University of Bristol, Bristol, UK

*Corresponding author: Joseph Asplet (joseph.asplet@bristol.ac.uk)

Observations of seismic anisotropy in the lowermost mantle — D″ — are abundant. As seismic anisotropy is known to develop as a response to plastic flow in the mantle, constraining lowermost mantle anisotropy allows us to better understand mantle dynamics. Measuring shear-wave splitting in body wave phases which traverse the lowermost mantle is a powerful tool to constrain this anisotropy. Isolating a signal from lowermost mantle anisotropy requires the use of multiple shear-wave phases, such as SKS and SKKS. These phases can also be used to constrain azimuthal anisotropy in D″: the raypaths of SKS and SKKS are nearly coincident in the upper mantle but diverge significantly at the core-mantle boundary. Any significant discrepancy in the shear-wave splitting measured for each phase can be ascribed to anisotropy in D″. We search for statistically significant discrepancies in shear-wave splitting measured for a dataset of 420 SKS-SKKS event-station pairs that sample D″ beneath the Eastern Pacific. To ensure robust results, we develop a new multi-parameter approach which combines a measure derived from the eigenvalue minimisation approach for measuring shear-wave splitting with an existing splitting intensity method. This combined approach also allows for easier automation of discrepant shear-wave splitting analysis. Using this approach we identify 30 SKS-SKKS event-station pairs as discrepant. These predominantly sit along a backazimuth range of $260° - 290°$. From our results we interpret a region of azimuthal anisotropy in D″ beneath the Eastern Pacific, characterised by null SKS splitting, and mean delay time of $1.15\,s$ in SKKS. These measurements corroborate and expand upon previous observations made using SKS-SKKS and S-ScS phase in this region. Our preferred explanation for this anisotropy is the lattice-preferred orientation (LPO) of post-perovskite. A plausible mechanism for the deformation causing this anisotropy is the impingement of subducted material from the Farallon slab at the core-mantle boundary.

Key words: Composition and Structure of the Mantle, Seismic Anisotropy, North America, Mantle Processes.

---

1 Introduction

The lowermost 200 km of the Earth's mantle, known as D$''$, is an important thermochemical boundary layer within the Earth, acting as a buffer between the liquid iron outer core and the solid silicate mantle. D$''$ is distinguished in some places from the lower mantle by a sharp vertical seismic discontinuity at the top of the layer (e.g., Lay and Helmberger, 1983; Sidorin et al., 1999,). Seismology is our primary source of information on this region of the Earth and it reveals a heterogeneous, anisotropic layer full of complexities which we do not fully understand (for example see reviews by Garnero et al., 2016; Romanowicz and Wenk, 2017).

Among these complexities are the dynamics of the lower mantle, and how they relate to the upper mantle and surface. For example, we know from seismic tomography that D$''$ is dominated by two large antipodal regions, beneath Africa and the Pacific, with anomalously low shear-wave velocities (e.g., Ritsema et al., 2011; French and Romanowicz, 2014; Auer et al., 2014; Moulik and Ekström, 2016). These large low shear-wave velocity provinces (LLSVPs) are widely considered to have crucial implications for the dynamics of the entire mantle. Despite advances in our understanding of LLSVP morphology (e.g., Cottaar and Lekic, 2016) the dynamics of LLSVPs and their relationship with deep mantle convection is still an open question (e.g., Davies et al., 2012; Garnero et al., 2016).

Seismic anisotropy is an indicator of long-range order in materials and in the upper mantle, it is known to develop as a response to plastic flow (e.g., Tommasi et al., 2000). In D$''$, seismic anisotropy has been attributed to several mechanisms. Lattice preferred orientation (LPO) of post-perovskite (pPv), a high pressure polymorph of bridgmanite (Br) at that is stable at D$''$ pressures (Murakami et al., 2004; Tateno et al., 2009), is an oft-invoked explanation (e.g., Wookey and Kendall, 2007). However there are outstanding questions surrounding the stability of pPv within D$''$. Due to the positive Clapeyron slope of the Br-pPv transition, pPv is most likely to be abundant in colder than average regions of D$''$ and non-existent in hot regions of D$''$ (Wookey et al., 2005b).

There is also the possibility of the steep geotherm near the core-mantle boundary causing a second crossing of the Clapeyron slope, resulting in lenses of post-perovskite in D$''$ bounded by bridgmanite (Wookey et al., 2005b; Hernlund et al., 2005).

LPO of post-perovskite is not the sole candidate mechanism for D$''$ anisotropy. Other minerals, such as bridgmanite, periclase or ferropericlase, are also capable of producing LPO anisotropy (e.g., Cordier et al., 2004; Marquardt et al., 2018). Alternatively, there are suggestions that D$''$ anisotropy occurs due to some shape preferred orientation (SPO) of heterogenieties, such as partial melt inclusions smaller than the seismic wavelength (e.g., Kendall and Silver, 1998; Kendall, 2000). Consequentially, improving our observational constraints of D$''$ anisotropy allows us to improve our knowledge of D$''$ dynamics, composition and temperature conditions.

Shear-wave splitting (or seismic birefringence) is a phenomena that arises as a response to seismic anisotropy (Crampin, 1985). When a shear-wave enters an anisotropic medium, the energy of the incident shear-wave is split into two orthogonally polarised quasi shear-waves. One wave (the fast shear-wave) is polarised in the direction of the fastest shear velocity, causing the quasi shear-waves to be separated by a delay time which persists beyond the causative anisotropic region. Shear-wave splitting is typically characterised by this delay time, δt, and the polarisation of the fast wave, referred to as the fast direction, ϕ, measured in the geographic reference frame as an azimuth relative to North.

Shear-wave splitting from upper mantle anisotropy has been extensively studied (see, for example, reviews by Silver, 1996; Savage, 1999) and is known to be a clear signature of seismic anisotropy. This makes it our best tool for studying anisotropy in D$''$, provided that we can account for anisotropy in the upper mantle. One way of achieving this is by using event-station pairs of different shear-wave phases. By carefully choosing the phases we use, we can take advantage of where their ray paths overlap and diverge in the mantle to account for upper mantle anisotropy.

Studies of D$''$ typical use either near-horizontally propagating phases (S, ScS, Sdiff) (e.g., Lay and Young, 1991; Wookey et al., 2005a; Maupin et al., 2005; Thomas et al., 2007; Nowacki et al., 2010) or more steeply incident, on the order of $\sim 20^\circ \sim 60^\circ$ depending on epicentral distance, phases (SKS, SKKS) (e.g., Niu and Perez, 2004; Restivo and Helffrich, 2006; Vanacore and Niu, 2011; Ford et al., 2015; Reiss et al., 2019) (Fig. 1). The limitations of using horizontally propagating phases is their long path length in D$''$, making it difficult to constrain the location of the observed anisotropy. Additionally, a lack of azimuthal coverage can restrict observations to vertical transverse isotropy (VTI), a geometry with a horizontal plane of isotropy with hexagonal symmetry. Given sufficient azimuthal coverage, this geometry can be generalised to allow for a tilted axis of symmetry (or tilted transverse isotropy, TTI) (e.g., Wookey and Kendall, 2008; Nowacki et al., 2010).

SKS and SKKS are radially polarised, as the core transiting P-wave only transmits a P and SV-wave into the mantle. This absence of SH-waves means that a VTI mantle will not produce shear-wave splitting in SKS and SKKS. Shear-wave splitting observed in these phases requires a more general form of anisotropy, such as azimithual anisotropy where there are azimuthal changes in velocity in the horizontal plane (Hall et al., 2004; Wookey and Kendall, 2007). This makes studying shear-wave splitting of SKS and SKKS ideal for constraining aziumthal anisotropy within D$''$. The ray paths of SKS and SKKS are almost coincident in the upper mantle and diverge by $\sim 800 km$ at the core-mantle boundary, for the epicentral distance range of $105^\circ - 140^\circ$ we consider here (Fig. 1). This significant deviation in D$''$ allows us to make the assumption that both SKS and SKKS sample the same different regions of D$''$. If we make the assumption that both SKS and SKKS sample the same upper mantle anisotropy, then any significant discrepancies in the shear-wave splitting measurements for these phases is best explained by a change in anisotropy between the two distinct domains of D$''$.

By comparing the shear-wave splitting measured for SKS and SKKS and testing if the measurements disagree in a statistically significant manner we can constrain the shear-wave splitting attributable to D$''$ (Niu and Perez, 2004). Where this is the case, we call the SKS-SKKS event-station pair 'discrepant'. Observations of discrepant

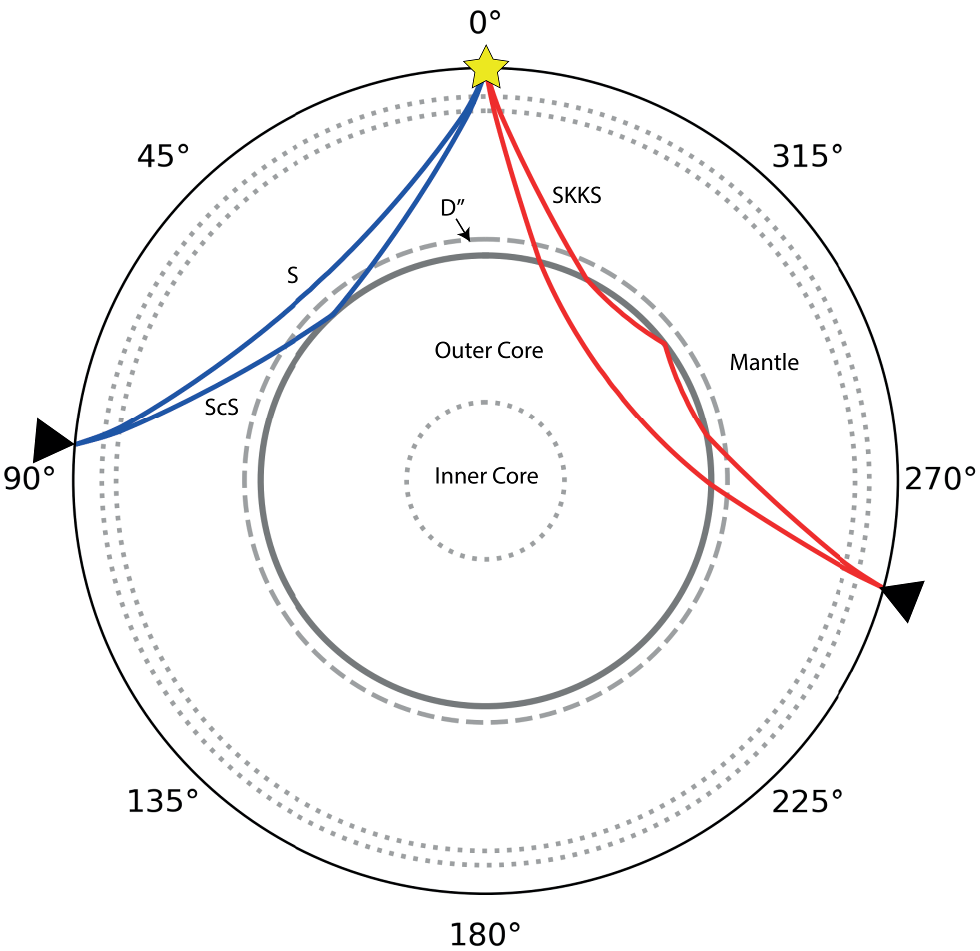

Figure 1: Raypaths of the phases (S, ScS, SKS and SKKS) typically used to study D″ anisotropy. Note the difference in the area of D″ sampled by ScS compared to that by SKS and SKKS. This allows for SKS and SKKS to sample D″ at a higher spatial resolution, although the shorter path length through D″ can result in a weaker shear-wave splitting signal. The divergence between SKS, SKKS raypaths through D″ is significant. At the shortest epicentral distances we consider ($\Delta = 105\,°$) SKS and SKKS exit the core approximately $700\,km$ apart, this distance increases with Δ. This significant deviation leads to the assertion that discrepant splitting between these two phases is best explained by anisotropy in D″ (e.g., Niu and Perez, 2004; Long, 2009; Reiss et al., 2019). Adapted from Nowacki et al. (2011).

SKS-SKKS shear-wave splitting are uncommon, with only $\sim 5\%$ of cases showing discrepancy attributable to D$''$ anisotropy in global studies (Niu and Perez, 2004; Restivo and Helffrich, 2006). Discrepant SKS-SKKS shear-wave splitting has been observed near the margin of the African (Wang and Wen, 2007; Lynner and Long, 2014; Ford et al., 2015; Long and Lynner, 2015; Grund and Ritter, 2018; Reiss et al., 2019) and Pacific (Long, 2009; Deng et al., 2017) LLSVPs and at the margin of the so-called 'Perm' anomaly (Long and Lynner, 2015). Given the importance of these observations in constraining azimuthal anisotropy in D$''$ and therefore the dynamics of the lowermost mantle it is vital to ensure results are robust.

We review current methods for identifying discrepant shear-wave splitting, testing existing approaches based on comparing estimated 2σ measurement uncertainties (e.g., Lynner and Long, 2014) and splitting intensity (Deng et al., 2017; Grund and Ritter, 2018; Reiss et al., 2019). We identify and demonstrate clear improvements that can be made to these methods using a set of synthetic split shear-waves and develop a new, multiparameter, approach to identifying discrepant shear-wave splitting. Using our new methods, we search for discrepant SKS-SKKS shear-wave splitting in the Eastern Pacific.

2 Methods - Identifying discrepant shear-wave splitting

2.1 Shear-wave splitting analysis

Shear-wave splitting is characterised by the polarisation direction of the fast wave, ϕ, and the delay time between the fast and slow waves, δt. There are several methods for measuring these parameters, such as cross-correlation (XC) (Bowman and Ando, 1987) and eigenvalue minimisation (EV) (Silver and Chan, 1991; Walsh et al., 2013).

We use the EV method implemented in the shear-wave splitting analysis code SHEBA, which incorporates the cluster analysis codes of Wuestefeld et al. (2010) (based on the code of Teanby et al. (2004)) to find the optimum analysis window, based on manually defined start and end ranges. This is done to ensure sufficient degrees of freedom for the splitting analysis.

Due to the near-vertical incidence angle of SKS, SKKS at the surface, we use the horizontal seismogram components only. This also removes the need to correct for free-surface coupling effects (Walpole et al., 2014). We perform a grid search over $0\,s \leq \delta t \leq 4\,s$ and $-90^\circ \leq \phi \leq 90^\circ$ and calculate the corresponding smallest eigenvalue of the trace covariance matrix, normalised by the largest eigenvalue. A shear-wave that has not experienced shear-wave splitting has a covariance matrix of rank 1, corresponding to the shear-wave energy being resolved wholly onto the radial component seismogram (Silver and Chan, 1991; Walsh et al., 2013). We denote this normalised eigenvalue as λ_2. By searching for splitting parameters that minimise λ_2 we invert for the apparent splitting operator $\Gamma_a(\phi, \delta t)$ applied to waveform as it propagates through the Earth. Where Γ_a represents the contributions from anisotropy in the upper mantle, Γ_{UM}, and in D$''$, $\Gamma_{D''}$, and satisfies the relation

$$\Gamma_{UM} \cdot \Gamma_{D''} \cdot \hat{\mathbf{p}} = K\Gamma_a \cdot \hat{\mathbf{p}} \tag{1}$$

where K is some complex scalar and $\hat{\mathbf{p}}$ is the initial polarisation direction (Silver and Savage, 1993).

The identification of un-split (or null) waveforms is an important part of shear-wave splitting analysis. Nulls occur either where the medium is isotropic, or if the initial shear-wave polarisation is near-parallel (or perpendicular) to the fast direction. In both cases we know that any δt value measured is meaningless, and if the medium is anisotropic that ϕ may indicate the fast or slow direction. We use an automated approach to detect nulls, using the parameter Q (Wuestefeld et al., 2010). This quality factor takes advantage of the systematic failure of the XC method for measuring shear-wave splitting close to null directions (Wüstefeld and Bokelmann, 2007; Wuestefeld et al., 2010). By comparing shear-wave splitting measurements made by the EV and XC methods and calculating the ratio of delay time measurements:

$$\Delta = \frac{\delta t_{XC}}{\delta t_{EV}} \tag{2}$$

and normalised differences in fast direction:

$$\Omega = \frac{(\phi_{EV} - \phi_{XC})}{45^\circ} \tag{3}$$

An idea 'good' measurement is defined by identical delay times and fast directions (i.e., $\Delta = 1, \Omega = 0$). For an ideal 'null' XC measurements show no delay time and the fast polarisation measurements differ by 45° (i.e., $\Delta = 0, \Omega = 1$). For an individual measurement, the qualitfy factor, Q, is calculated from the distance to these ideal cases:

$$d_{null} = \sqrt{\Delta^2 + (\Omega - 1)^2}\sqrt{2} \tag{4}$$

$$d_{good} = \sqrt{\Delta - 1)^2 + \Omega^2}\sqrt{2} \tag{5}$$

$$Q = \begin{cases} -(1 - d_{null}), \text{for } d_{null} \leq d_{good} \\ (1 - d_{good}), \text{for } d_{null} \geq d_{good} \end{cases} \tag{6}$$

Therefore Q ranges from -1 (a clear null), through 0 (poor), to +1 (a clear split). We use a cutoff of $Q > 0.7$ for split events or $Q < -0.7$ for nulls.

2.2 Splitting Intensity

Splitting intensity (SI), an alternate measure of shear-wave splitting, has become increasingly popular for differential splitting studies of D$''$ (e.g., Deng et al., 2017; Grund and Ritter, 2018). The principle advantage of splitting intensity is that it is a commutative (Chevrot, 2000), something that is not true of splitting operators (e.g., Silver and Savage, 1993; Silver and Long, 2011). Therefore the contribution from D$''$

can be recovered by taking the difference of the SI measured for SKS and SKKS. The limitation of splitting intensity is that we do not individually resolve the direction or strength of D$''$ anisotropy, but a combination of the two.

Splitting intensity is defined by the amplitude of the transverse component, **T**, relative to the time derivative of the radial component, $\dot{\mathbf{r}}$. If the signal-to-noise ratio is low, the optimal estimate of SI is obtained by projecting the transverse component onto the time derivative of the radial component (Chevrot, 2000) yielding:

$$SI = -2\frac{\mathbf{T}\dot{\mathbf{r}}}{||\dot{\mathbf{r}}^{\mathbf{2}}||} \tag{7}$$

where $||\dot{\mathbf{r}}^{\mathbf{2}}|| = \dot{\mathbf{r}}^{\mathbf{t}}\dot{\mathbf{r}}$ is the squared norm of $\dot{\mathbf{r}}$.

Assuming a simple case of a homogeneous anisotropic layer, SI can also be approximated as a re-parameterisation of $\phi, \delta t$ (Chevrot, 2000). If we assume that δt is small relative to the dominant period of the incoming wavelet $w(t)$, we can express $\dot{\mathbf{r}}$ and **T** as:

$$\dot{\mathbf{r}} \approx w'(t) \tag{8}$$

and

$$\mathbf{T} \approx -\frac{1}{2}(\delta t sin2\beta)w'(t) \tag{9}$$

where β if the difference between the fast direction, ϕ, and the source polarisation of the wave. As SK(K)S phases are radially polarised when they exit the core, we assume that the source polarisation is equal to the backazimuth of the wave. From (8), (9) it is clear that:

$$SI \approx \delta t sin(2\beta) \tag{10}$$

This approximation for splitting intensity is used in recent splitting intensity studies of discrepant SKS-SKKS shear-wave splitting (e.g., Deng et al., 2017; Grund and Ritter, 2018; Reiss et al., 2019). In discrepant splitting studies, the absolute difference in splitting intensity,

$$\Delta SI = |SI_{SKS} - SI_{SKKS}| \tag{11}$$

is taken (Deng et al., 2017). The periodicity of the approximation (eqn. 10) introduces potential problems of non-uniqueness where a large range of $(\phi, \delta t)$ return the same ΔSI value. This effect is demonstrated when we model ΔSI using synthetic split shear-waves.

Another potential issue arises from the definition of a null, a shear-wave which is not split, in splitting intensity. A null is defined where $SI \approx 0$. When the splitting intensity approximation is made, this is not always the case. This arises from the grid search methods employed to measure $\phi, \delta t$. The approximation for SI assumes that in the case of a null $\delta t \approx 0s$. In the presence of noise δt can often be unconstrained, with $\delta t \rightarrow 4s$ in the grid search (Fig. 2). This issue is mitigated in recent studies (e.g., Deng et al., 2017; Reiss et al., 2019) through manual inspection of the SKS and SKKS waveforms, examining the linearity of the particle motion to visually confirm null measurements.

With the size of splitting datasets ever increasing, improving our measurements of splitting intensity to remove the requirement to visually inspect all null waveforms is preferable. Here we present an adjustment to the method for measuring SI, implementing the trace component projection as set out in equation 7. This removes the need to make the approximation and is computationally inexpensive and allows for easier automation of discrepant shear-wave splitting analysis. This also has the added advantage of making our splitting intensity measurements independent of our measured splitting parameters.

2.3 Robust identification of discrepant shear-wave splitting

The conventional approach for identifying discrepant shear-wave splitting is to compare $\phi, \delta t$ for each phase allowing for their estimated 2σ uncertainties (e.g., Lynner and Long, 2014). We use the estimated Gaussian uncertainties in $\phi, \delta t$ (Silver and Chan, 1991; Walsh et al., 2013) and test whether the two splitting measurements sit within

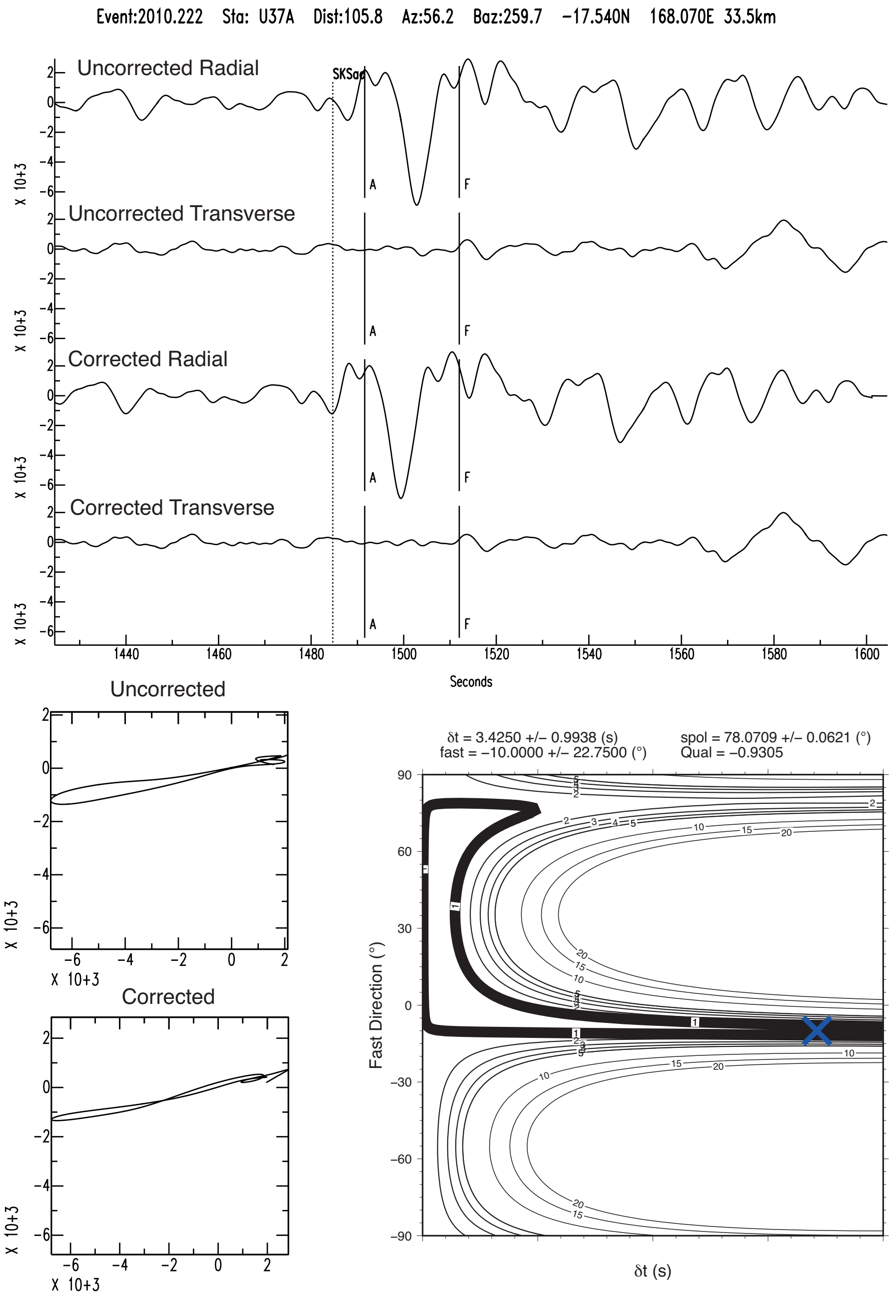

Figure 2: A null SKS phase at station U37A as measured by SHEBA (see supplementary figure S1 for an SKKS example). Here we show the uncorrected and corrected traces (top) and particle motions (below left), along with the eigenvalue surface (below right). Note how the grid search algorithm has moved across towards the maximum δt. This trend is seen throughout our dataset.

these bounds. Whilst this approach is reasonable, it is limited by the approximation used to convert the F-test defined 95% confidence region of the λ_2 surface into the more useful individual parameter uncertainties $\sigma_\phi, \sigma_{\delta t}$ (Silver and Chan, 1991). Inspection of λ_2 measurement surfaces for a set of results quickly reveals that the 95% confidence region is seldom regular (Fig. 3)

This estimation of uncertainties has the potential to introduce regular error into the process of identifying discrepant shear-wave splitting. In particular there is a tendency for over-estimation of $\sigma_\phi, \sigma_{\delta t}$ (implying a lower confidence in the result). In turn, this can result in false identification of matching SKS-SKKS shear-wave splitting. In our new approach, we have developed an improved strategy to avoid these potential errors.

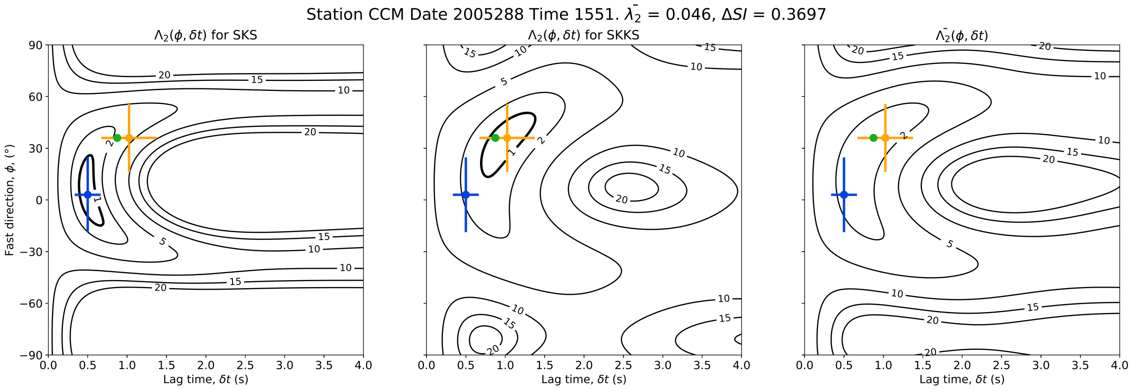

Figure 3: Λ_2 surfaces output by SHEBA when measuring shear-wave splitting in SKS (left) and SKKS (center). The bold contour line bounds the 95% confidence region. The right panel shows that stacked surface $\bar{\Lambda}_2$. The minimum λ_2 for SKS (blue) and SKKS (orange) are plotted over all 3 surfaces along with the estimated 2σ uncertainties in $\phi, \delta t$. The minimum value of $\bar{\Lambda}_2$, $\bar{\lambda}_2$, is shown in green. In this example $\bar{\lambda}_2$ is less than the sum of the 95% confidence regions for SKS and SKKS (eqn. 12) and the measurements are classified as matching.

When measuring shear-wave splitting using eigenvalue minimisation, we apply our grid search over $\phi, \delta t$ and compute λ_2 at each node. This creates a surface, which we denote $\Lambda_2(\phi, \delta t)$. In conventional shear-wave splitting analysis we are only concerned with the minimum value of this surface. However, $\Lambda_2(\phi, \delta t)$ contains information which can help us test for discrepant splitting. Instead of characterising these misfit surfaces with Gaussian uncertainties $\sigma_\phi, \sigma_{\delta t}$, we use all the information contained within them. This allows us to avoid errors made in the assumptions required to obtain $\sigma_\phi, \sigma_{\delta t}$.

We achieve this by summing $\Lambda_{2SKS}(\phi,\delta t)$ and $\Lambda_{2SKKS}(\phi,\delta t)$, to produce a new surface $\bar{\Lambda_2}(\phi,\delta t)$ (Fig. 3). This new surface effectively describes how well each $\Gamma(\phi,\delta t)$ works as a solution for both phases. Therefore by taking the best fitting value of $\bar{\Lambda_2}$, which we denote $\bar{\lambda_2}$, we have a measure that can be used to determine whether the best fitting splitting solutions for each phase are discrepant.

To robustly identify discrepant shear-wave splitting, we need to account for uncertainty in our splitting measurements and define what we consider to be statistically significant differences between the solutions for SKS and SKKS. We calculate the λ_2 value that bounds the 95% confidence region in $\Lambda_2(\phi,\delta t)$ for each phase, $\lambda_2^{95\%}$, using an F-test as set out in Silver and Chan (1991). We sum these two values, defining a threshold for $\bar{\lambda_2}$ that we can test against. By comparing $\bar{\lambda_2}$ to the sum of $\lambda_2^{95\%}$ for SKS and SKKS we can determine if the splitting measurements are discrepant. If:

$$\bar{\lambda_2} > \lambda_{2_{SKS}}^{95\%} + \lambda_{2_{SKKS}}^{95\%} \tag{12}$$

then the shear-wave splitting measured for SKS and SKKS is classified as discrepant.

3 Synthetics

To test our approach, and to demonstrate some of the pitfalls in the various methodologies, we model $\bar{\lambda_2}$ and ΔSI in $\phi,\delta t$ space using synthetic shear-waves. We generate synthetics over a range of $0s \leq \delta t \leq 4s$ at intervals of $0.25s$ and $-90^\circ \leq \phi \leq 90^\circ$ at intervals of 5°, producing a evenly spaced grid of 629 synthetics (Fig. 4a). We generate synthetics for source polarisations of $30^\circ, 45^\circ$ & 60°. For clarity, we show results here from synthetics generated with a source polarisation of 45°. Random noise is added to the synthetics to mimic conditions for real data. For each source polarsiation we generate synthetics with a high signal-to-noise ratio (SNR), where $SNR \approx 37$, and with a low SNR, where $SNR \approx 10$. Shear-wave splitting is measured using SHEBA. The

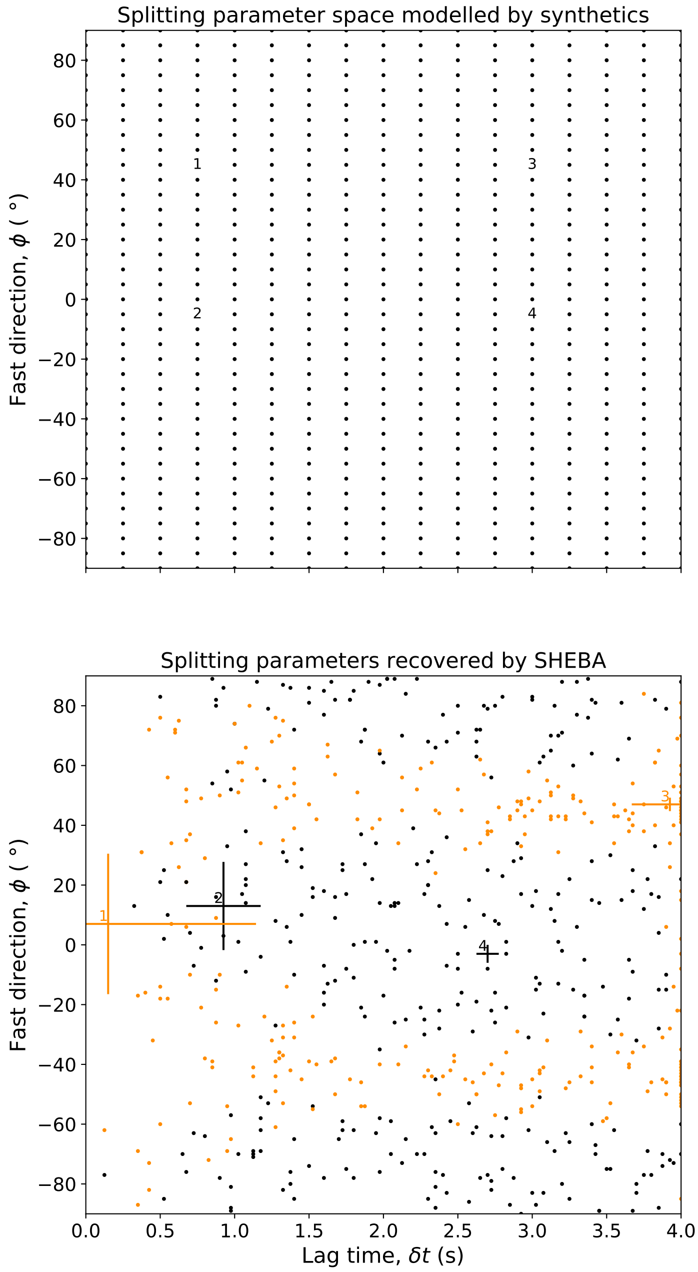

Figure 4: (Top) The initial grid of synthetic shear-waves, with a source polarisation of 45°. (bottom) Shear-wave splitting parameters measured by SHEBA for the set of synthetics shown above. Synthetics that are identified as nulls by the quality factor, Q (Wüstefeld and Bokelmann, 2007), are plotted in orange. Where $Q = -1$ this indicates a clear null and $Q = 1$ this indicates a clear split shear-wave. We use a threshold of $Q \leq -0.7$ to identify nulls. We highlight 4 example points (numbered) across both panels to track the migration of our synthetics from their input position to the measured splitting parameters. For null points this effect is significant, with most nulls with a low input δt being migrated along the source polarisation direction. Note source polarisation and fast direction do not need to directly align for a null to be recorded, even at a low signal-to-noise ratio. The majority of synthetics with a fast direction within 10° of the source polarisation axis are returned as nulls.

measured splitting parameters for the synthetics (Fig. 4b) and the $\Lambda_2(\phi, \delta t)$ surfaces produced by SHEBA are used to test the performance of the different measures of discrepant shear-wave splitting.

To create synthetic event-station pairs, we select a single synthetic split shear-wave and denote it as 'SKS'. We then denote the whole grid of 629 synthetics as 'SKKS' and construct a set of 629 'SKS-SKKS' pairs. This allows us to visualise all possible sets of event-station pairs and the behaviour of different measures of discrepant shear-wave splitting (Fig. 5) across the parameter space. For these synthetic SKS-SKKS pairs we search for discrepant splitting using 2σ error bar matching (Fig. 5a), our new measure $\bar{\lambda_2}$ (Fig. 5b,6b) and ΔSI using both the approximation for spitting intensity from measured splitting parameters (Fig. 5c,6c) and the full projection approach (Fig. 5d,6d).

Our synthetics demonstrate the error that can be introduced when using 2σ error bar matching (Fig. 5a, 6a) . This is primarily restricted to nulls, where the shape of the error surface produces high estimates of $\sigma_\phi, \sigma_{\delta t}$ and thus spurious matches are found. This is expressed as false classification of matching splitting where $\delta t \approx 0s$ and along the source polarisation axis (45 °) and its antipode (-45 °).

Our new measure, $\bar{\lambda_2}$, performs similarly to the 2σ method. This is to be expected given our method is a refinement of 2σ. However, unlike the 2σ method, our new measure clearly defines a single region of matching shear-wave splitting and does not show the same susceptibility to false classification of nulls. At a high signal-to-noise ratio the matching regions for $\bar{\lambda_2}$ and 2σ are both very tightly bound (Fig. 5b). As SNR decreases, this breaks down for both measures, as the noise expands the 95% confidence region in shear-wave splitting analysis. Synthetics generated at lower, more realistic, SNRs show this and that $\bar{\lambda_2}$ is more narrowly constrained (Fig. 6a,b). This occurs as at lower signal-noise ratios $\Lambda_2(\phi, \delta t)$ tend to have 95% confidence regions which are not well fit by the rectangular approximation used to obtain $\sigma_\phi, \sigma_{\delta t}$.

Our synthetics results also highlight inherent non-uniqueness in ΔSI (Fig. 5c,d). Our results also clearly show the difference between measuring splitting intensity by approximation (Fig. 5c) and by projection (Fig. 5d). Both measures of splitting intensity define a broad region where $\Delta SI < 0.4$, although the region does not exhibit the same level of instability as $2\sigma and \bar{\lambda_2}$ as SNR decreases (Fig. 6c,d).

These results clearly show that none of these measures alone are ideal for identifying discrepant shear-wave splitting. For example, splitting intensity difference even at high SNR does not define a regular matching region in $\phi, \delta t$ space when compared to $\bar{\lambda_2}$. At lower SNR ratios this difference is less pronounced, as increasing noise makes discrepant shear-wave splitting more difficult for all methods to resolve.

3.1 Discussion

Our synthetics results demonstrate that there are problems with all measures of discrepant shear-wave splitting when used individually. Our new measure of discrepant shear-wave splitting does offers improvement, but comes with its own pitfalls. It is clear that measuring SI using the projection method offers improvement over approximating SI from the splitting parameters $\phi, \delta t$. The apparent non-uniqueness in ΔSI that we have identified (Fig. 5c,d) raises a potential issue in this approach that requires careful treatment in discrepant shear-wave splitting analysis.

When we compare methods for measuring splitting intensity for real data (Fig. 7) we confirm the issues suggested by the synthetic analyses, along with a broader disagreement between methods for split phases (Fig. 7a). This disagreement, particularly when we consider that the splitting intensity test for discrepancy relies on the difference between measurements, highlights that improvement can be made by using the full projection method.

Our new $\bar{\lambda_2}$ test does not have the same non-uniqueness issues as ΔSI, however it is strongly dependant on the signal-to-noise ratio of the data. When we explore its performance across $\phi, \delta t$ space with our synthetics, we see that $\bar{\lambda_2}$ defines a single, well-constrained region where we can classify the shear-wave splitting as matching. By

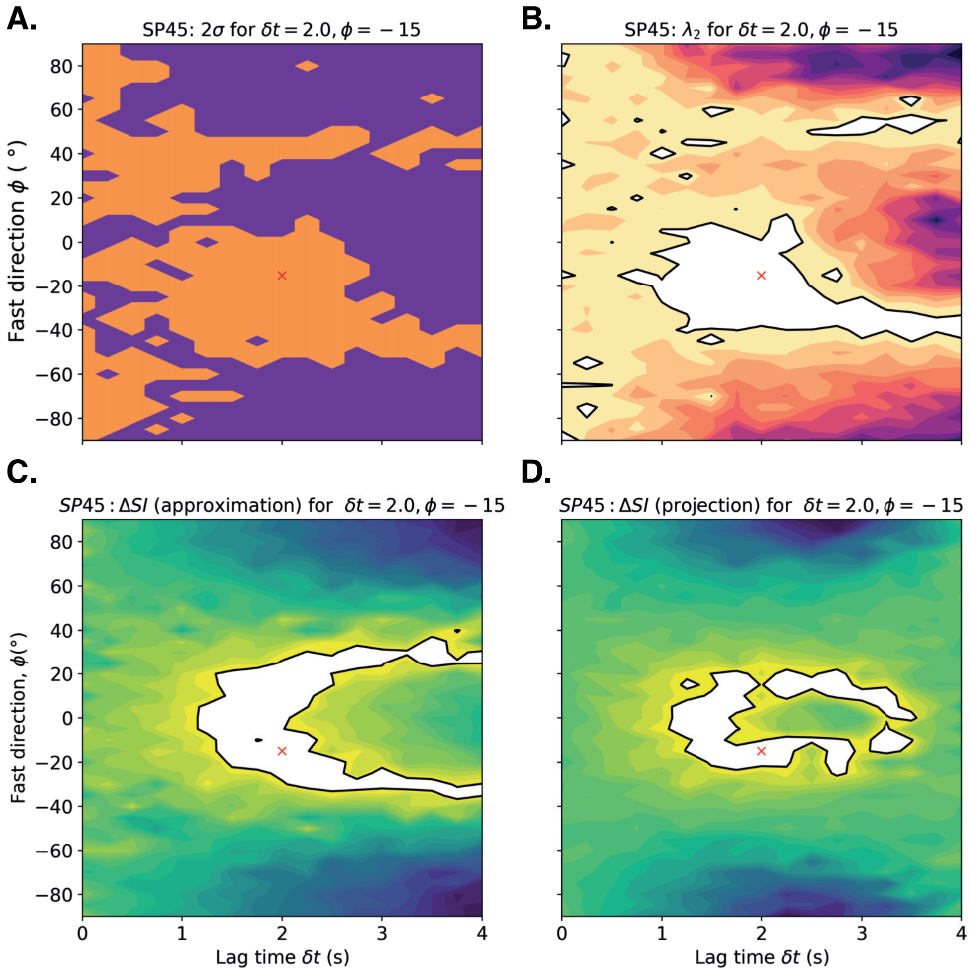

Figure 5: Synthetics grid with a source polarisation of 45°, synthetic pairs are constructed by "pairing" the result at grid position $\delta t = 2.0\,s, \phi = -15^\circ$ (red cross) with all other points in the grid. Splitting measures for each synthetic pair are plotted at the position of the input $\phi, \delta t$ for the synthetic 'SKKS'. A) Classification using 2σ where orange indicates matching pairs and purple discrepant pairs. B) $\bar{\lambda}_2$ contoured for all pair in the grid. The purple line encloses the region where $\bar{\lambda}_2 < 1.15(\lambda_2^{SKS} + \lambda_2^{SKKS})$. C,D) ΔSI for splitting intensity measure by approximation (C.) and by projection (D.). The region in white indicates where $\Delta SI \leq 0.4$ the threshold suggested by Deng et al. (2017).

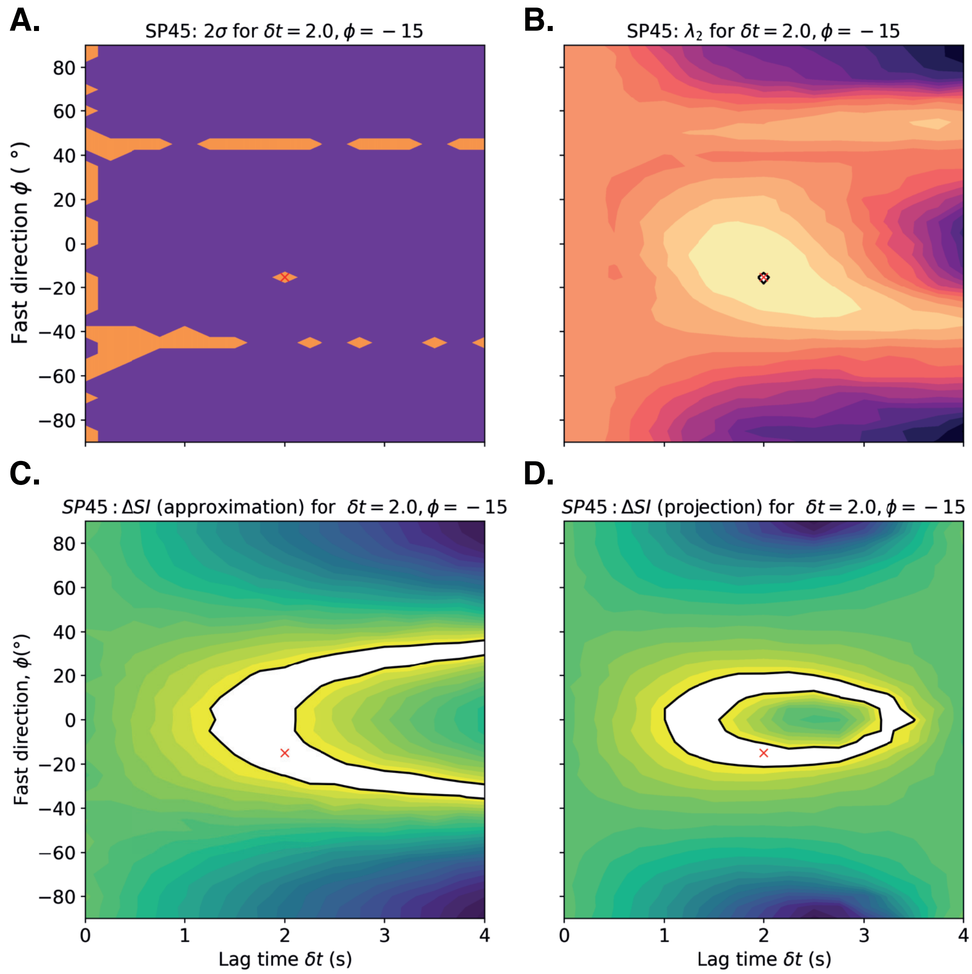

Figure 6: The same as Figure 5 with a random white noise added such that the mean SNR of the synthetics is now ≈ 10. Synthetic pairs are constructed by "pairing" the result at grid position $\delta t = 2.0s, \phi = -15^\circ$ (red cross) with all other points in the grid. Splitting measures for each synthetic pair are plotted at the position of the input $\phi, \delta t$ for the synthetic 'SKKS'. A) Classification using 2σ where orange indicates matching pairs and purple discrepant pairs. B) $\bar{\lambda_2}$ contoured for all pair in the grid. The purple line encloses the region where $\bar{\lambda_2} < 1.15(\lambda_2^{SKS} + \lambda_2^{SKKS})$. C,D) ΔSI for splitting intensity measure by approximation (C.) and by proejction (D.). The region in white indicates where $\Delta SI \leq 0.4$ the threshold suggested by Deng et al. (2017).

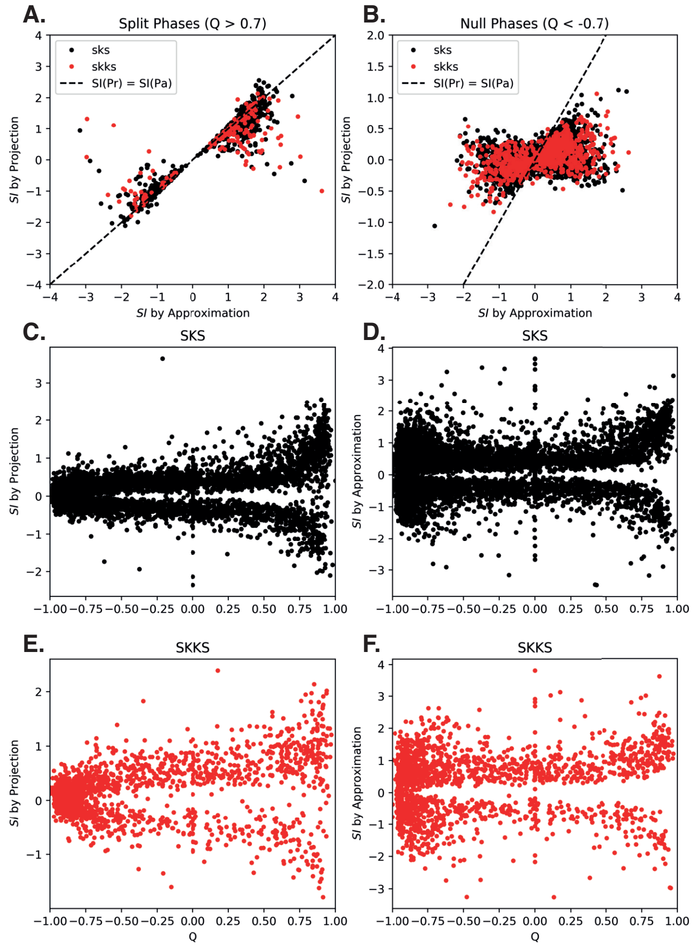

Figure 7: Splitting Intensity calculated using an approximation (Pa) (Chevrot, 2000; Deng et al., 2017) and the projection (Pr) (Chevrot, 2000). A) the projected and approximated SI for all the split phases in our dataset B) projected and approximated SI for all nulls. Note the contrast in spread of the two measures, where approximation ranges from -3 to 3 whilst projection most events are between -0.5 and 0.5. For a null, splitting intensity should be ≈ 0. C,E) Splitting intensity by projection against Q for SKS and SKKS respectively. D,F) Splitting intensity by approximation against Q for SKS and SKKS respectively. A Q of -1 indicates a clear null and a Q of 1 indicates a clear split shear-wave. This result can also be reproduced using our synthetics (supplemental figure S6)

summing the estimated 95% confidence λ_2 values (Silver and Chan, 1991) for SKS and SKKS we define a criteria for $\bar{\lambda}_2$ which scales with uncertainty in the individual measurements. A drawback is that these uncertainties increase with noise, which reduces the efficacy of $\bar{\lambda}_2$ when the signal-to-noise ratio is low. The matching region defined by $\bar{\lambda}_2$ broadens and in some cases can break down, reducing our ability to resolve discrepant shear-wave splitting. This is an important restriction as the signal-to-noise ratio is often relatively low (~ 8.0) for SKS and SKKS. Relying solely on either $\bar{\lambda}_2$ or ΔSI opens us to the risk of their pitfalls. These pitfalls can be somewhat mitigated where there is visual inspection of all waveforms (e.g., Deng et al., 2017; Reiss et al., 2019).

We know that SKS and SKKS are not sensitive to VTI anisotropy (Hall et al., 2004), which is a common approximation used when modelling anisotropy in D″ (e.g., Walker et al., 2011). We also know that discrepant splitting between these phases has to be explained by non-VTI anisotropy from D″, which requires us to invoke models of D″ anisotropy with lower symmetry. Therefore it is paramount that we have confidence that our observations of discrepant SKS-SKKS shear-wave splitting are accurate and robust.

In the low-SNR environment we are often forced to work in studying SKS-SKKS shear-wave splitting, the relative stability of ΔSI makes it a good complementary measure to $\bar{\lambda}_2$. The measures are complimentary to each other and combining them in a multiparameter approach helps to mitigate their drawbacks. Our $\bar{\lambda}_2$ test solves an issue of inherent non-uniqueness in the ΔSI method, and ΔSI resolves the issues with the broadening region of $\bar{\lambda}_2 \leq (\lambda_{2_{SKS}}^{95\%} + \lambda_{2_{SKKS}}^{95\%})$ as signal-to-noise ratio decreases. Measuring splitting intensity using projection (Chevrot, 2000) decouples ΔSI from $\bar{\lambda}_2$. This gives us two independent measures to test for discrepant shear-wave splitting.

We suggest that applying both the ΔSI (where SI is measured using projection) and our $\bar{\lambda}_2$ test, gives us the most robust means for identifying discrepant SKS-SKKS shear-wave splitting. Using this multiparameter approach will allow for easier automation of discrepant shear-wave splitting analysis.

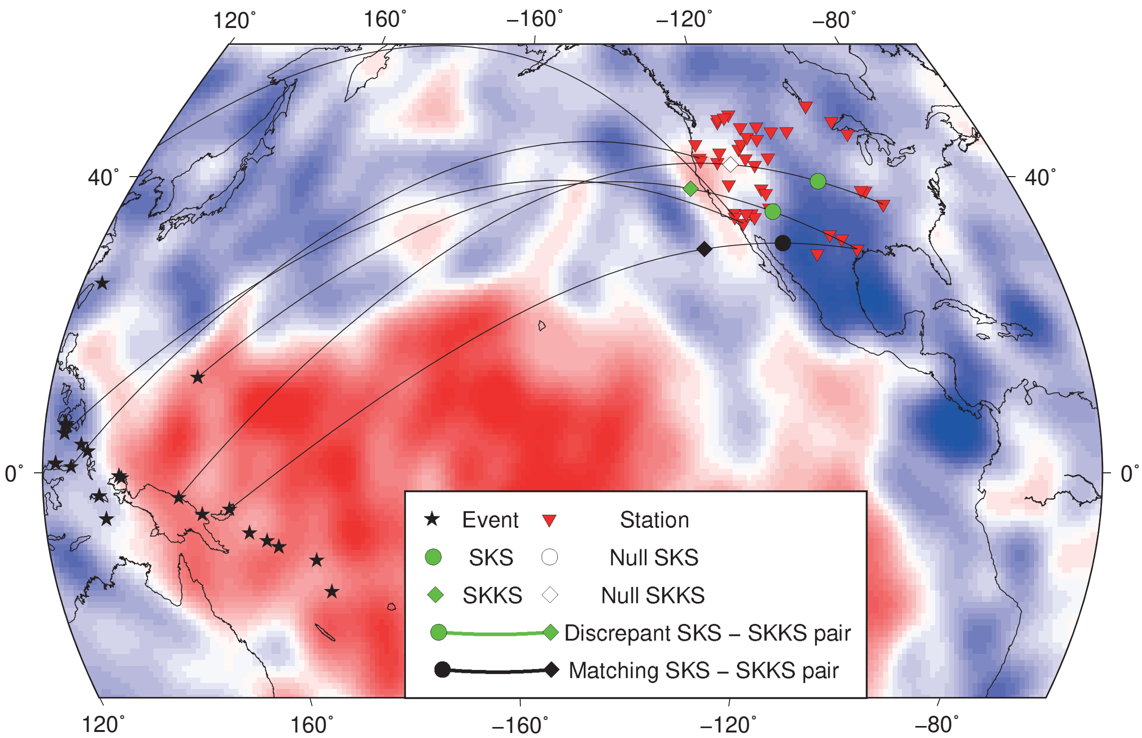

Figure 8: Event locations (stars) and stations (triangles) used to produce our Eastern Pacific dataset. Example raypaths taken by SKS, SKKS are drawn, with SKS and SKKS pierce points through the core-mantle boundary indicated by circles and diamonds respectively. This is plotted over the isotropic shear-wave velocity at the base of the mantle from the model S40RTS (Ritsema et al., 2011), show as a % deviation from the reference model.

4 Multi-parameter discrepant splitting analysis, a case study.

4.1 The NE Pacific region

To test our new, multi-parameter, approach to identifying discrepant SKS-SKKS splitting, we construct a dataset of SKS-SKKS event station pairs. Whilst the full dataset has a global scope, we focus our analysis on a subset of SKS-SKKS pairs recorded at stations in the North Eastern Pacific (Fig. 8). This region contains several features in D″ that we might expect to result in azimuthal anisotropy. This makes it an ideal region to search for discrepant SKS-SKKS shear-wave splitting.

The nearby strong lateral gradient in shear-wave velocity, associated with the margin of the Pacific LLSVP (Fig. 8) is one such feature. Recent studies have found that azimuthal anisotropy is concentrated at or near to the margins of the African LLSVP (Cottaar and Romanowicz, 2013; Lynner and Long, 2014; Ford et al., 2015), the Perm anomaly (Long and Lynner, 2015) and southern margins of the Pacific LLSVP (Deng et al., 2017; Creasy et al., 2017).

Previous studies of the Eastern Pacific using SKS-SKKS (Long, 2009) and S-ScS (Nowacki et al., 2010) have found evidence for azimuthal anisotropy in D″. This anisotropy, particularly the TTI anisotropy modelled by (Nowacki et al., 2010), is attributed to deformation of D″ surrounding subducted Farallon slab material. However the limited coverage of these studies leaves the full extent of this anisotropy unconstrained. By revisiting this region with a new SKS-SKKS dataset, we demonstrate the effectiveness of our new technique whilst also improving our constraints on D″ anisotropy.

4.2 Data

We construct our dataset from a previous dataset of SKS shear-wave splitting results by Walpole et al. (2014). We select a subset of these results that are clearly identified as being either split or null according to their quality factor, Q (Wuestefeld et al., 2010). We use a cutoff of $Q > 0.7$ for split events or $Q < -0.7$ for nulls. For the 954 events selected where we could also pick SKKS, we download broadband seismic data from the IRIS data management centre. All events are processed using SHEBA, where we measure $\phi, \delta t$, along with splitting intensity by both approximation and projection.

Shear-wave splitting in SKS and SKKS are measured independently. Prior to our analysis we detrend and demean the seismograms and check for data gaps or spikes. We filter all seismograms with a two-pass two-pole butterworth bandpass filter, with corner frequencies of 0.01 Hz and 0.5 Hz. We chose a upper corner frequency of 0.5 Hz in order to better resolve weakly split ($\delta t \approx 0.5$ s) phases. Excluding these higher frequencies can lead to weakly split phases being measured as nulls (Walpole et al., 2014). This is especially important as these weakly split results tend to occur at "null" stations where there is no apparent anisotropy in the upper mantle.

After performing shear-wave splitting analysis we remove events with a signal-to-noise ratio ≤ 5. Additionally we reject phases with a difference in backazimuth and source polarisation $\geq 10°$. For all SKKS phases, we then identify the SKS result for the same event and combine them to produce SKS-SKKS event-station pairs. This results in a dataset of 420 SKS-SKKS pairs with upwards core-mantle boundary pierce points in the Eastern Pacific. Additionally, we use our full dataset to test the performance of measuring splitting intensity by approximation and projection.

4.3 Results

Following our synthetic examples we test for discrepant SKS-SKKS splitting in our Eastern Pacific data using both $\bar{\lambda_2}$ and ΔSI. The 111 pairs where both phases are null

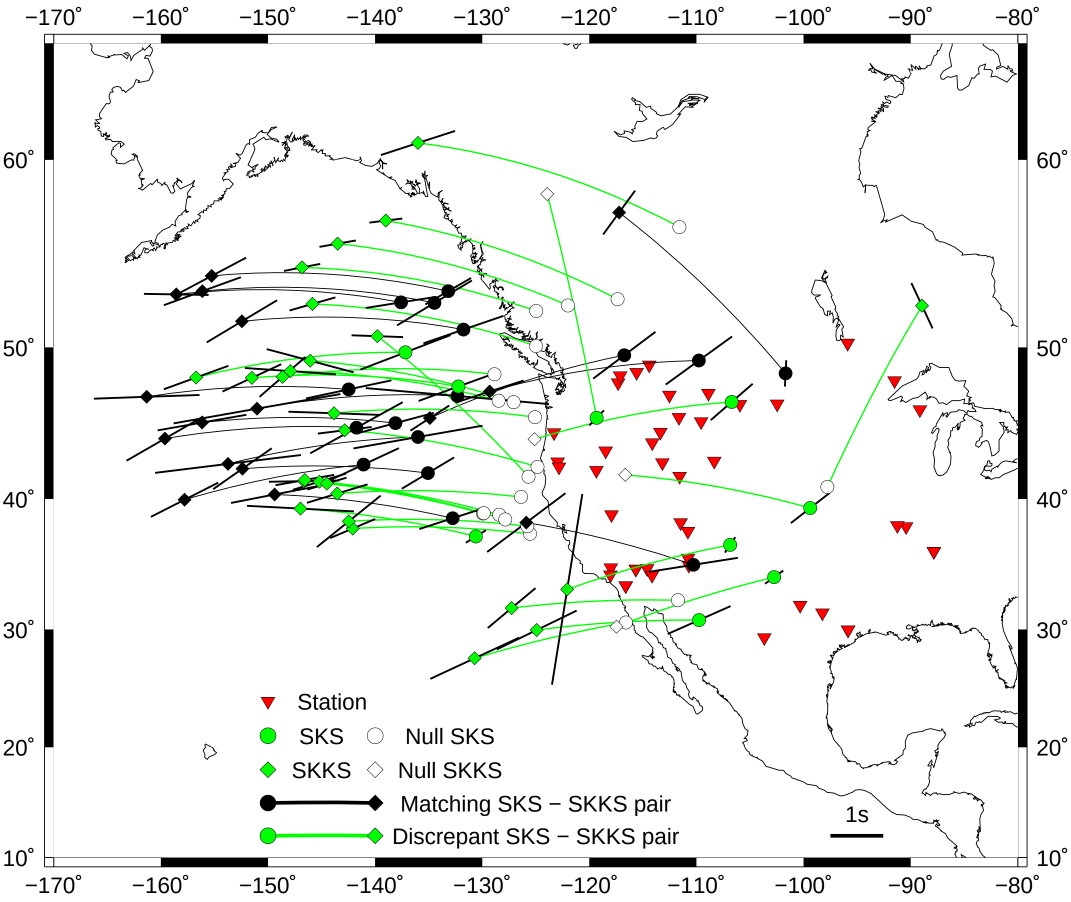

Figure 9: Matching and discrepant SKS-SKKS pairs where at least one phase has been split. SKS-SKKS event station pairs are classified as either matching (black) or discrepant (green) using our new measure $\bar{\lambda}_2$ and a modified ΔSI test (see text). SKS (circle) and SKKS (diamond) results are plotted at their up-going pierce points at the core-mantle boundary. These are calculated using TauP (Crotwell et al., 1999) assuming an IASP91 1-D velocity model (Kennett and Engdahl, 1991). For phases that are split, the associated parameters are drawn as bars oriented ϕ° from N with a length proportional to δt at the corresponding piercing point. For each event station pair SKS and SKKS piercing points are connected with a great circle arc. These connecting arcs are also coloured according to whether the pair is interpreted as matching (black) or discrepant (green). Null-split pairs are inferred as discrepant as in other studies (e.g., Grund and Ritter, 2018).

and the 256 where one phase has a Q factor between -0.5 and 0.5, are discarded from our analysis.

After we apply our multiparameter discrepancy test ($\bar{\lambda}_2$ and ΔSI by projection) to the remaining 53 pairs, we find that 30 show discrepant SKS-SKKS splitting (Fig. 9). Of the discrepant pairs, there are 5 cases where both SKS and SKKS are split. The remaining 25 discrepant pairs are cases where one phase (usually SKS) is null and the other is clearly split. The majority of the pairs follow a backazimuth of $260° - 290°$, with no clear correlation between backazimuth and discrepant splitting. We also see a few discrepant SKS-SKKS pairs at other backazimuths, but these events are too isolated to make any meaningful interpretation. We focus on the 48 SKS-SKKS pairs with pierce points between $\sim -160°$and $\sim -120°$ longitude and between $\sim 35°$and $\sim 60°$ latitude. We see that discrepancy is primarily correlated to longitude and that our splitting results are broadly consistent with latitude (Fig. 9). The most striking feature is the north-south line of 18 discrepant pairs with a null SKS and a split SKKS occurring at longitudes of $\sim -130°$ to $\sim -120°$. The measured splitting in SKKS for these event-station pairs has a mean δt of $1.15s \pm 0.02s$ and mean splitting intensity of 0.93 ± 0.05. There are 3 discrepant SKS-SKKS pairs in this sub-region where both phases are split. We also note that we only have two stations, FRD and ULM, where we see both null and split SKS.

Moving further West, we see a more complex transition to pairs which are discrepant, but with splitting in both SKS and SKKS, and then to where both phases return matching splitting. In contrast to the null-split pairs, the 12 matching event-station pairs here have a mean δt of $1.72s \pm 0.07$ and mean SI of 1.35 ± 0.11 for SKS and a mean δt of $1.80s \pm 0.03s$ and a mean SI of 1.24 ± 0.12 for SKKS. This increase in splitting is what we expect to observe as the null SKS phase in a null-split pair indicates that there is no contribution to shear-wave splitting from the upper mantle. Our observations of interspersed matching and discrepant SKS-SKKS pairs is broadly consistent with previous work in this region (Long, 2009), where anomalous SKS-SKKS splitting was observed along a similar backazimuth range further to the south (Fig. 9).

We also investigate the measured splitting intensity across our global dataset, to further explore the contrast between approximating SI and using the projection method. Our results (Fig. 7) again show the disagreement between the two methods. Separating split (Fig. 7a) and null (Fig. 7b) phases shows that the splitting intensity approximation is inaccurate in both cases, whilst we only expected it to perform poorly for nulls. Plotting the measured splitting intensities against the quality factor Q, an indicator of nulls, for SKS (Fig 7c,d) and SKKS (Fig 7e,f) also demonstrates the large range of splitting intensities returned for nulls by the approximation. It is also worth noting that these result can be also be reproduced using synthetic shear-waves (Supplemental figure S6). This systematic discrepancy between approximated and projected splitting intensity suggests that approximated splitting intensity should be used with caution and where possible should be replaced with splitting intensity measured by projection.

5 Azimuthal Anisotropy in D$''$ beneath the Eastern Pacific

Our results in the Eastern Pacific show that, in line with other studies (e.g., Niu and Perez, 2004; Restivo and Helffrich, 2006), discrepant SKS-SKKS shear-wave splitting is uncommon, but resolvable. The clear observation of discrepant SKS-SKKS splitting near the edge of the Pacific LLSVP continues a global trend where discrepant SKS-SKKS shear-wave splitting has been observed at, or near, margins of the Pacific (Deng et al., 2017) and African (Lynner and Long, 2014; Reiss et al., 2019) LLSVPs and near the Perm anomaly (Long and Lynner, 2015). Our results corroborate and expand upon previous SKS-SKKS results in this region (Long, 2009), where a similar pattern of discrepant splitting was seen along a similar backazimuth range further South (Fig. 9). This is indicative a province in D$''$ that exhibits azimuthal anisotropy. By including the observations of Long (2009), we can extend this interpretation further, covering a large province of D$''$ near the Eastern margin of the Pacific LLSVP across which we can

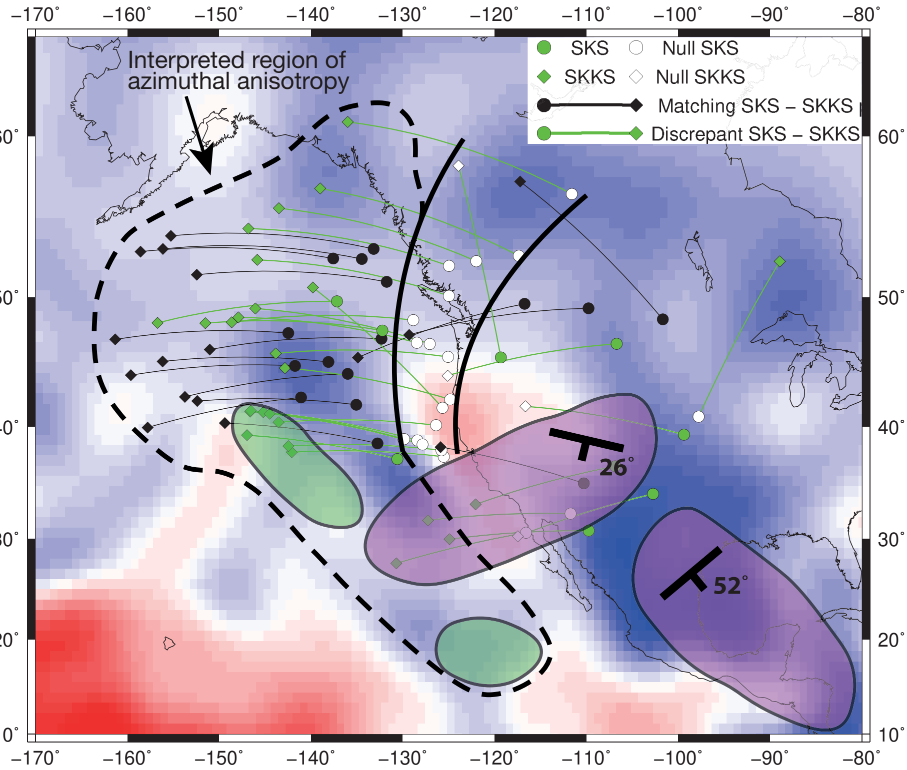

Figure 10: Matching and discrepant SKS-SKKS event-station pairs where at least one phase has been split, plotted over the S40RTS isotropic shear-wave velocity model at the core-mantle boundary (Ritsema et al., 2011). SKS (circle) and SKKS (diamond) results are plotted at their up-going pierce points at the core-mantle boundary. These are calculated using TauP (Crotwell et al., 1999) assuming an IASP91 1-D velocity model (Kennett and Engdahl, 1991). Our interpreted region of potential azimuthal anisotropy in D″ is shown by the dashed line. The solid lines denote where we see the change in anisotropy in D″ from our observation of null-split SKS-SKKS pairs. Previous studies of D″ anisotropy in this region are shown using SKS-SKKS (green bubbles) (Long, 2009) and S-ScS (purple) (Nowacki et al., 2010). The orientation and dip of the tilted transverse isotropy (TTI) modelling by Nowacki et al. (2010) is also shown.

interpret a change in seismic anisotropy (Fig. 9).

Our observations of null SKS phases, paired with split SKKS, demark where this change in anisotropy occurs. The clear north-south trend of SKS-SKKS null-split pairs over $\sim 20°$ latitude is best explained by a change in D$''$ anisotropy. The weaker splitting parameters for the SKKS phases in these null-split pairs, compared to the nearby matching split SKS-SKKS pairs, suggests that these pairs do not sample any upper mantle anisotropy and instead SKKS is solely sampling azimuthal anisotropy in D$''$. This change in D$''$ anisotropy could be a simple rotation of the anisotropic medium between the regions sampled by SKS and SKKS, such that SKS is no longer sensitive to it due to alignment of the medium's fast direction and the polarisation of SKS. Alternatively there could be a change across this region, either to a different anisotropic mechanism or to isotropy.

We have no similar constraint on the westward extent of this region. Indeed, a plausible explanation for the transition from discrepant to matching SKS-SKKS shear-wave splitting is the province of azimuthal anisotropy is large enough that the more westerly pairs are both sampling the azimuthal anisotropy. This best explains why our result are so closely interspersed, with the SKKS pierce points of the null-split sampling the same region of D$''$ as many of our matching pairs. This province of azimuthal anisotropy must be broadly homogeneous, as we would expect any significant lateral variations within the region to also produce widespread discrepant SKS-SKKS shear-wave splitting whereas we only see 3 SKS-SKKS pairs in this region that are discrepant where both phases are split.

A strong candidate for this azimuthal anisotropy is LPO of post-perovskite (pPv), extending away from the Pacific LLSVP (Fig. 10). Post-perovskite is known to be stable in the pressure and temperature conditions of the lowermost mantle (Murakami et al., 2004) and is often favoured by observational and modelling studies of D$''$ anisotropy (e.g., Walker et al., 2011; Ford et al., 2015; Creasy et al., 2017).

An interpretation of pPv requires a decrease in temperature to affect the phase transition

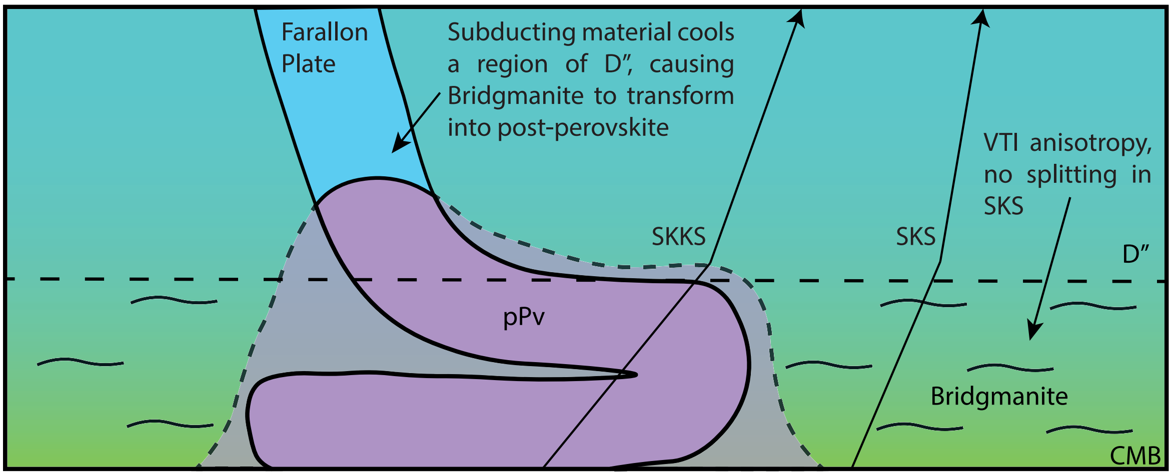

Figure 11: Summary cartoon of our interpretation of a post-perovskite ridge in D″. The cold Farallon slab collects along the core mantle boundary (following numeric models (e.g., Mcnamara et al., 2002)). In the pressure conditions of D″ and due to the positive claperyon slope (Murakami et al., 2004) this cold material crosses the phase transition to post-perovskite. The cooling effect of the collecting slab material may also sufficiently cool the surrounding native D″ material to extend the post-perovskite ridge. The surrounding D″ material must be isotropic or anisotropic with VTI in order to explain the consistent observations of null SKS phases.

from bridgmanite (Murakami et al., 2004). This is consistent with the body-wave tomography-derived shear-wave velocity (Fig 9), as faster velocities are attributed to colder regions of in D″. These faster regions of the lowermost mantle are often inferred to be associated with subducted slab material. Plate motion models (Richards and Lithgow-Bertelloni, 1998) suggest the Farallon plate has reached the core-mantle boundary in this region and previous work invokes this as a probable cause of D″ anisotropy (Long, 2009). As the cold subducted material reaches the core-mantle boundary the pressure conditions become sufficient for bridgmanite to transition to post-perovskite. The cooling effect of the collecting slab material may also sufficiently cool the surrounding native D″ material to expand the post-perovskite province away from the slab.

As pPv has different elastic properties to bridgmanite, we do not require a change in lowermost mantle deformation across this region to explain our observations. However, we would expect for there to be deformation associated with the subducting Farallon slab. We may be detecting this with our 4 discrepant SKS-SKKS pairs where both phases are split, however they are too disparate to draw any meaningful interpretation.

Further data colleciton, especially an improvement in backazimuthal coverage, is needed to search for slab-associated deformation. Our observed trend of null-split pairs with a nulls SKS and split SKKS suggests a change in D″ anisotropy across the region. This could be explained by a change in deformation of D″ causing a rotation of the anisotropic medium, resulting in the SKS null. Alternatively we could be seeing an East-West transition from pPv to bridgmanite, where bridgmanite then does not produce anisotropy that SKS is sensitive to (Fig. 11).

Whilst LPO of post-perovskite is a strong candidate mechanism, other mechanisms cannot be ruled out. Bridgmanite and ferropericlase, the other two significant lowermost mantle minerals can generate significant anisotropy through LPO (e.g., Cordier et al., 2004; Marquardt et al., 2018). However both phases are ubiquitous throughout the lower mantle, which is generally considered to be isotropic away from D″ (Meade et al., 1995). This makes these phases less plausible explanations that post-perovskite. An SPO mechanism also cannot be ruled out. SPO models of layered disc-like or tubular melt inclusions have been shown to generate anisotropy very efficiently, requiring a very low volume-fraction (< 0.0001 of melt (Kendall and Silver, 1998)) to manifest a measurable signal.

Distinguishing between these candidate mechanism has thus far been a significant challenge to our understanding of D″. Indeed, SPO and LPO may yet prove to be complementary mechanisms, depending on the length scale of deformation within D″ with respect to the seismic wavelengths used. Recent forward modelling efforts (Ford et al., 2015; Creasy et al., 2017; Pisconti et al., 2019) have improved our constraints on D″ anisotropy, although most candidate mechanisms produce plausible results. Further expansion of these methods to remove the reliance on single-crystal elastic tensors, along with improving our observational constraints through the integration of ScS, SKS and SKKS shear-wave splitting data with reflected PdP and SdS polarities (Creasy et al., 2019) will allow to greatly improve our understanding of D″ anisotropy.

6 Conclusions

We have shown using both synthetics and real data that if not carefully treated, current methods for identifying discrepant shear-wave splitting have limitations that may lead to both false positive and negative results. To ensure robust detection and analysis of discrepant shear-wave splitting we have developed a new measure derived from the eigenvalue minimisation method used to measure shear-wave splitting for each phase. Additionally, we propose some improvements to the measurement of spitting intensity and its application to discrepant splitting analysis. Combining these independent measures in multiparameter approach allows us to more rigorously test for discrepant shear-wave splitting and for easier automation of discrepant shear-wave splitting analysis . This allows us to use SKS-SKKS shear-wave splitting data to constrain D'' anisotropy with improved confidence.

Our SKS-SKKS results in the Eastern Pacific suggest a region of azimuthal anisotropy in D'', near the Eastern margin of the Pacific LLSVP. We also see a change in D'' anisotropy across this region, requiring a change in mechanism or in D'' deformation. Our observations are best explained by lattice preferred orientation of post-perovskite, where the change in anistropy is potentially due to post-perovskite transitioning to bridgmanite. Our preferred model to achieve these conditions in D'' is the impingement of material from the Farallon slab near the core-mantle boundary. Future studies combining SKS-SKKS and S-ScS shear-wave splitting data using complementary backazimuth ranges, along with intensive forward modelling of predicted D'' anisotropy, should help to further improve our understanding of anisotropy of this part of D'', and its links to the dynamics of the Earth system.

7 Acknowledgements

We would like to thank Jack Walpole and Andy Nowacki for their comments and insight which has helped improve the quality of this manuscript. JA is supported by a

NERC GW4+ Doctoral Training Partnership studentship from the Natural Environment Research Council [NE/L002434/1] and by a postgraduate grant from the Government of Jersey. Maps were produced using GMT (Wessel and Smith, 1995). SHEBA is available at http://www.github.com/jwookey/sheba .

8 Supplementary Figures

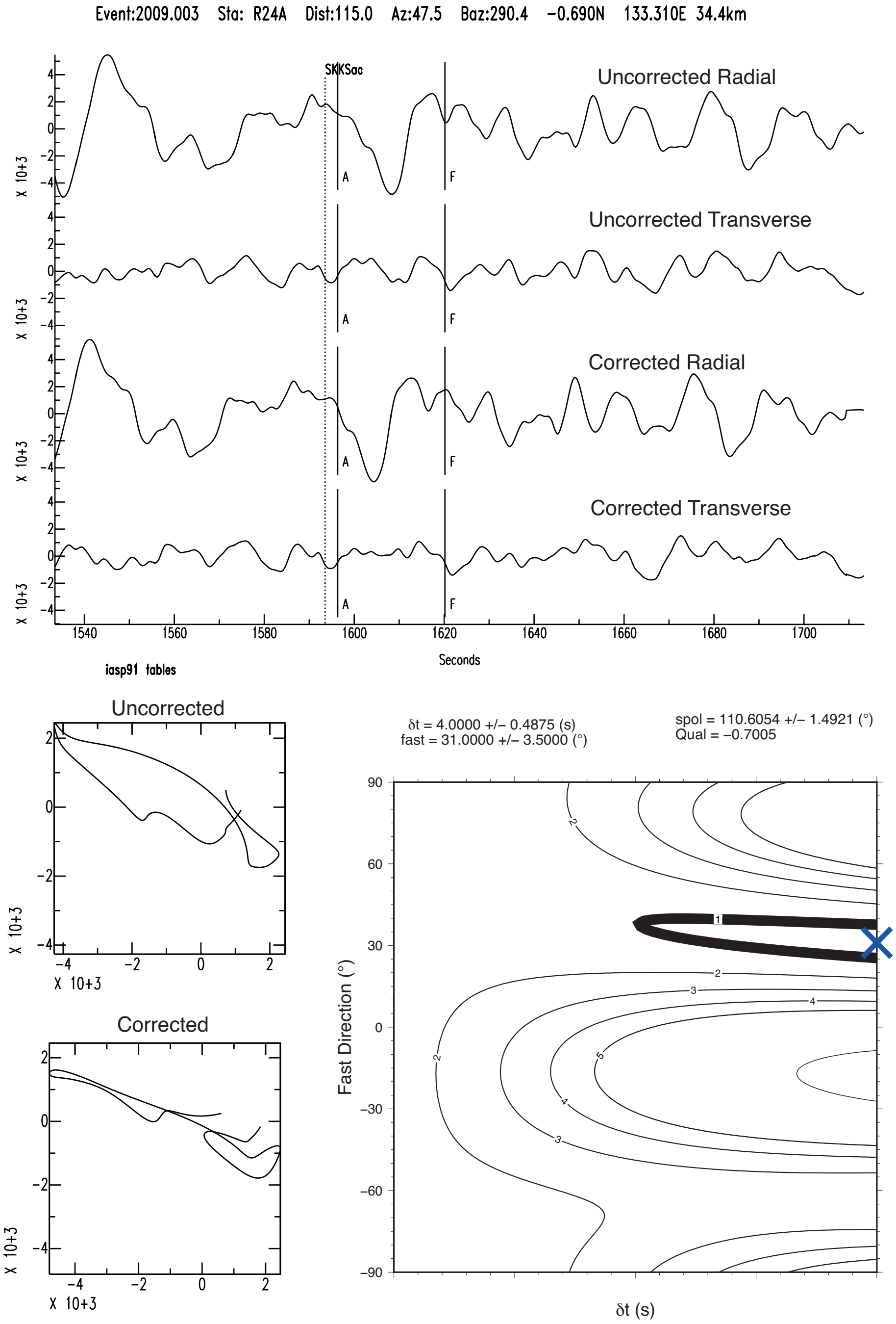

Figure S1: A null SKKS phase at station R24A as measured by SHEBA (see figure 2 for an SKS example). Here we show the uncorrected and corrected traces (top) and particle motions (below left), along with the eigenvalue surface (below right). This example has the highest Q value of all identified nulls used in our study, a classification that is easily confirmed when inspected the particle motion and eigenvalue surface. Note how the grid search algorithm has moved across towards the maximum δt. This trend is seen throughout our dataset.

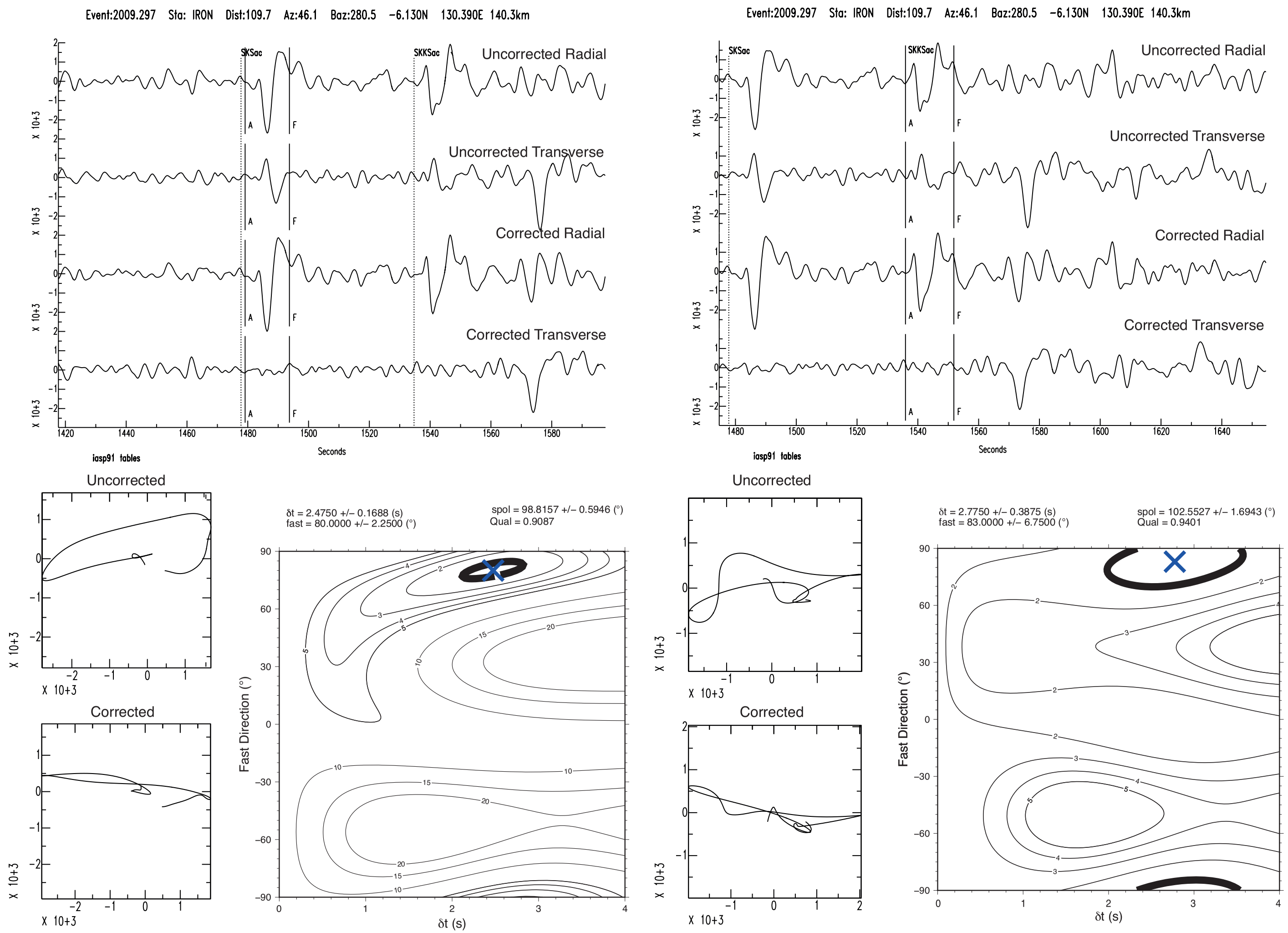

Figure S2: A matching SKS-SKKS event-station pair recorded at station IRON. This case shows an example where $\Delta SI = 0.59$, which would classify this pair as discrepant. By including our $\bar{\lambda}_2$ test we instead classify this pair as matching, which is evident from the agreement of the splitting parameters

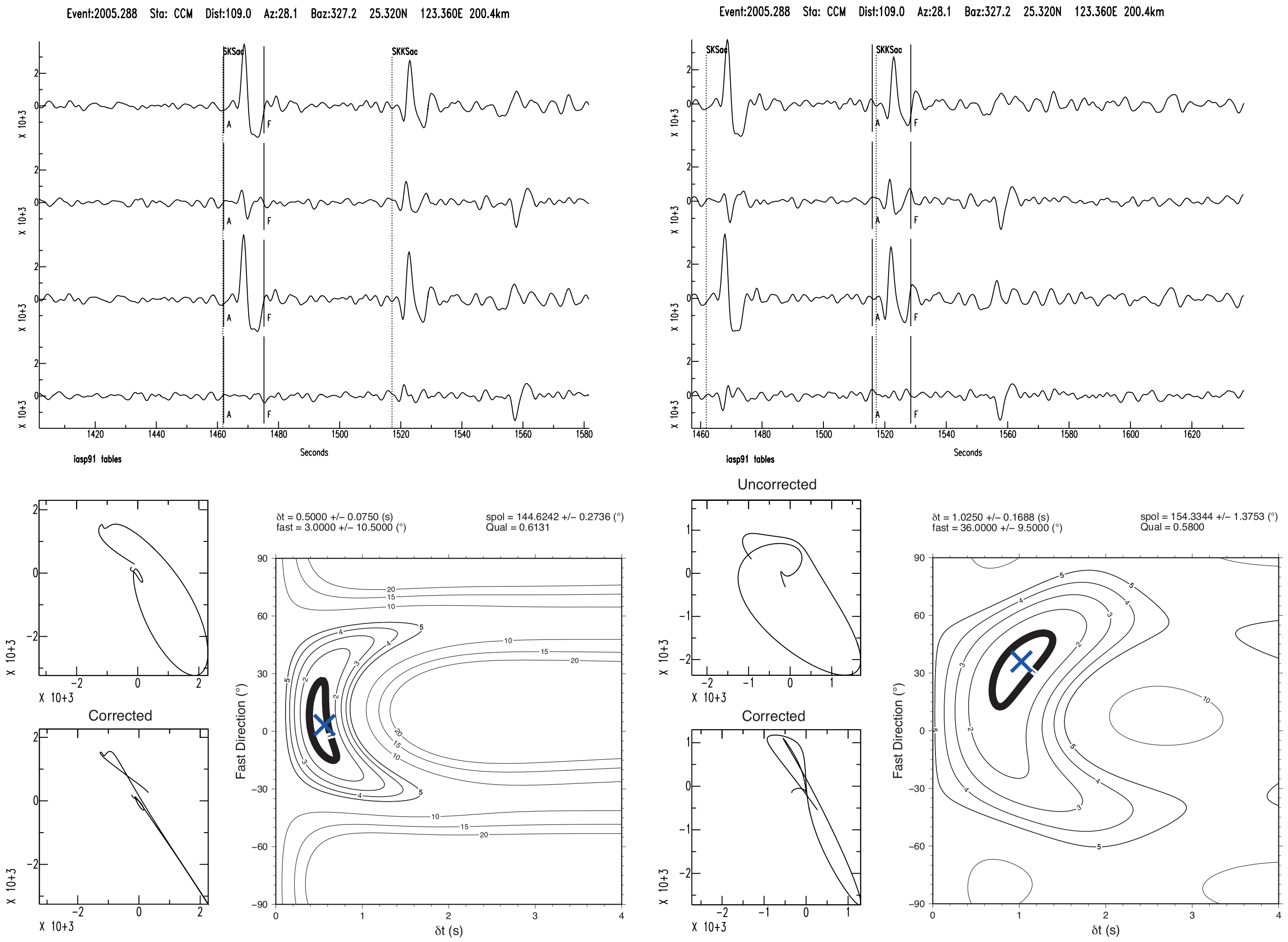

Figure S3: A matching SKS-SKKS event-station pair recorded at station CCM. In this case $\bar{\lambda}_2 = 0.046$ and is greater than sum of the two 95% confidence levels, $\lambda_2^{95\%} = 0.042$. This suggests that the pair is discrepant. However for this example $\Delta SI = 0.29$, resulting in the pair being classified as matching. In this case there is a source polarisation discrepancy of $\approx 10°$ and the SNR of SKKS (8.3) is much less than that of SKS (17.9). With this we are not confident that this example can be classified as discrepant and is an example of where ΔSI is complimentary to $\bar{\lambda}_2$

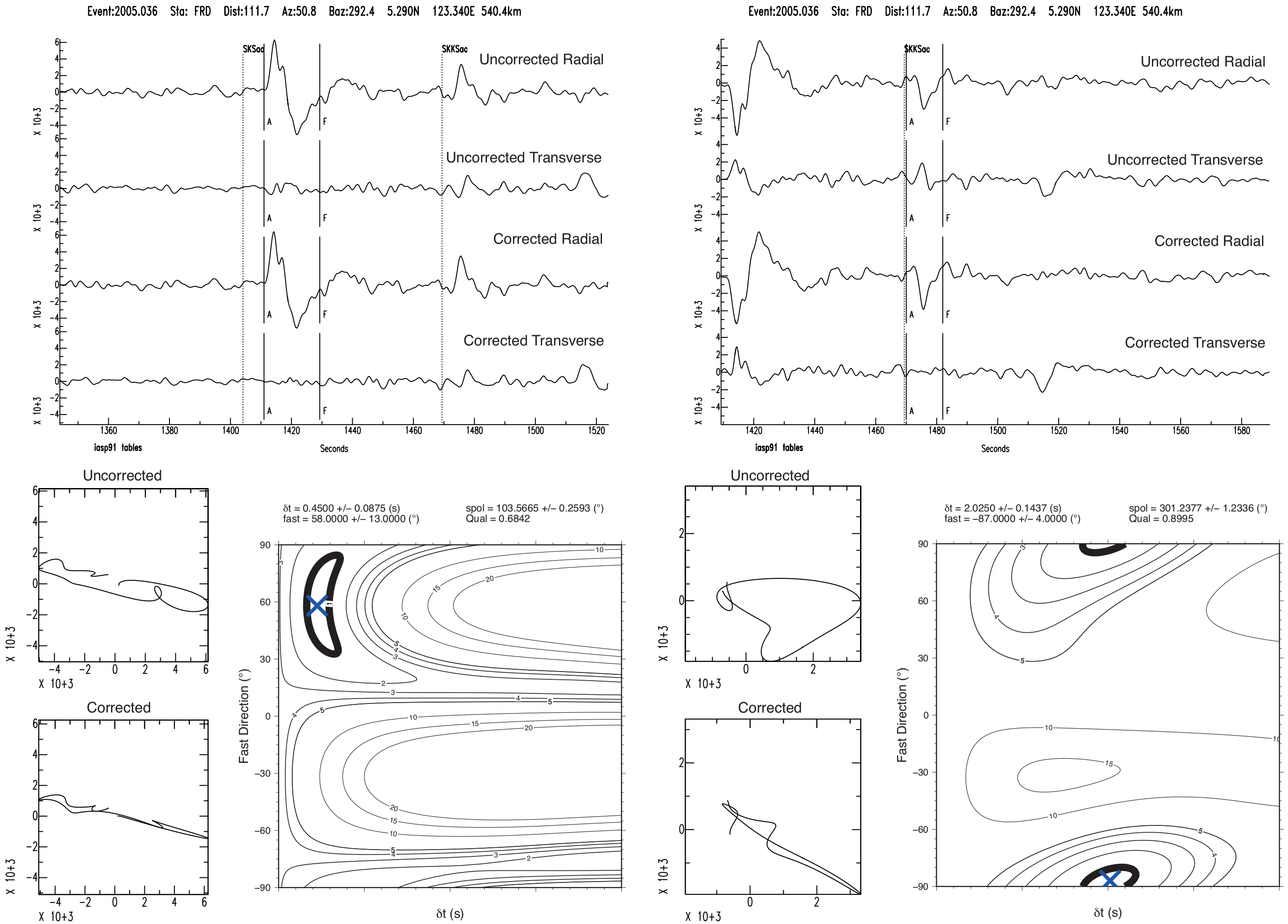

Figure S4: A discrepant SKS-SKKS event-station pair recorded at station FRD. Here we show the uncorrected and corrected traces and particle motions, along with the eigenvalue surface for SKS (left) and SKKS (right). This is the most extreme example of discrepant shear-wave splitting recorded in our dataset. In this example $\Delta SI = 0.78$ and $lam\bar{b}da_2 = 0.035$ which is greater than the sum of the two 95% confidence levels, $\lambda_2^{95\%} = 0.033$

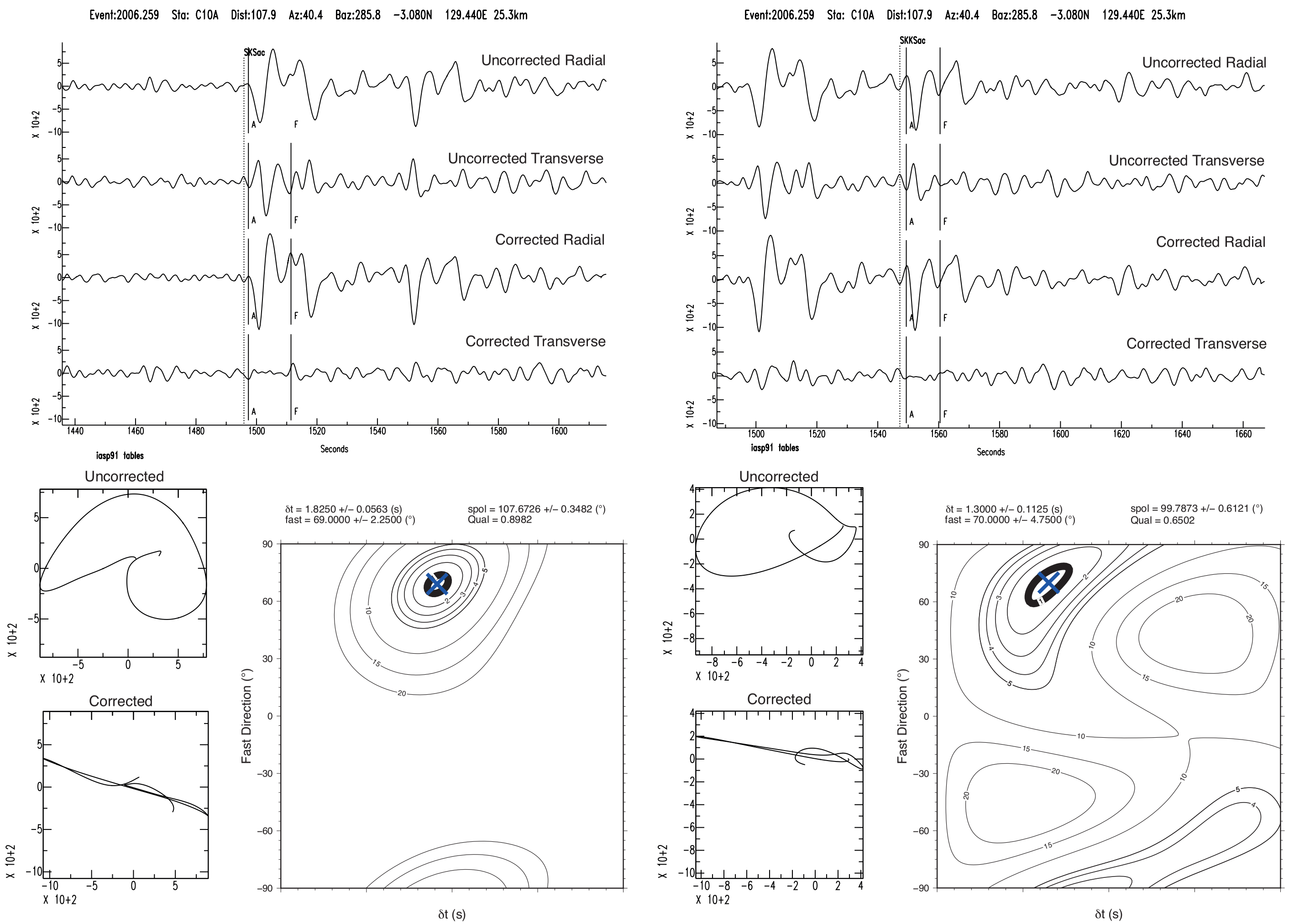

Figure S5: A discrepant SKS-SKKS event-station pair recorder at station C10A. Here we show the uncorrected and corrected traces and particle motions, along with the eigenvalue surface for SKS (left) and SKKS (right). The discrepancy in this example is significantly smaller compared to SFS4 and more typical of the other discrepant split pairs we observe. Whilst the discrepancy appears small it is clearly identified by both measures, with a $\Delta SI = 0.89$ and $\bar{\lambda}_2 = 0.037$ which is much greater than the sum of the two 95% confidence levels, $\lambda_2^{95\%} = 0.022$ the result is interesting as we would typically expect SKS (left) to have a smaller delay time than SKKS (right) as SKKS has a longer path in D″.

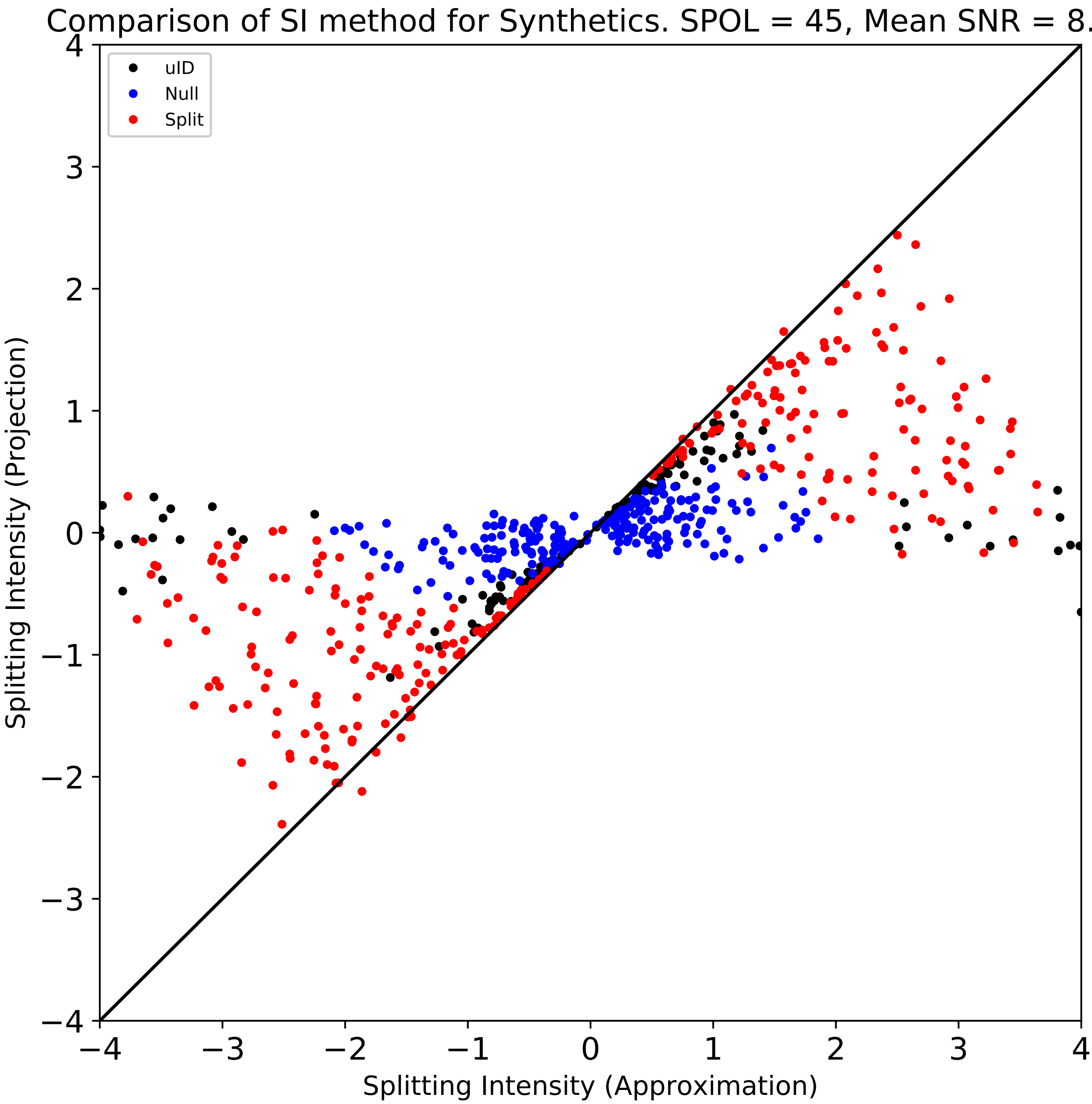

Figure S6: A reproduction of Figure 7A, comparing Splitting Intensity calculated using an approximation (Pa) (Chevrot, 2000; Deng et al., 2017) and the projection (Pr) (Chevrot, 2000), using synthetics. The synthetics used here are the same as those used to test our discrepancy measures and are generated on a evenly spaced grid of 629 synthetic split shear-waves over a range of $0 \leq \delta t \leq 4s$ and $-90 \leq \phi \leq 90°$, with a mean SNR of ≈ 8. Synthetics are coloured base on their classification by Q (Wuestefeld et al., 2010) (see text). Splits synthetics (Q ¿ 0.5) are shown in red, null synthetics (Q ¡ -0.5) are shown in blue and synthetics where $0.5 \leq Q \leq 0.5$ are shown in black. The solid line shows $SI(Pr) = SI(Pa)$, which we would expect most of the results to sit near if the approximation is accurate.

References

Auer, L., Boschi, L., Becker, T. W., Giardini, D., 2014. Savani : A variable resolution whole-mantle model of anisotropic shear velocity variations based. Journal of Geophysical Research: Solid Earth, 3006–3034.

Bowman, J. R., Ando, M., 1987. Shear-wave splitting in the upper-mantle wedge above the Tonga subduction zone J. Geophysical Journal of the Royal Astronomical Society 88 (March), 25–41.

Chevrot, S., 2000. Multichannel analysis of shear wave splitting. Journal of Geophysical Research: Solid Earth 105 (B9), 21579–21590.

Cordier, P., Ungar, T., Zsoldos, L., Tichy, G., 2004. Dislocation creep in MgSiO3 perovskite at conditions of Earth's uppermost lower mantle. Nature 428, 837 – 840.

Cottaar, S., Lekic, V., 2016. Morphology of seismically slow lower-mantle structures. Geophysical Journal International 207 (2), 1122–1136.

Cottaar, S., Romanowicz, B., 2013. Observations of changing anisotropy across the southern margin of the African LLSVP. Geophysical Journal International 195 (2), 1184–1195.

Crampin, S., 1985. Evaluation of anisotropy by shearwave splitting. GEOPHYSICS 50 (1), 142–152.

Creasy, N., Long, M. D., Ford, H. A., 2017. Deformation in the lowermost mantle beneath Australia from observations and models of seismic anisotropy. Journal of Geophysical Research: Solid Earth 122 (7), 5243–5267.

Creasy, N., Pisconti, A., Long, M. D., Thomas, C., Wookey, J., 2019. Constraining lowermost mantle anisotropy with body waves: A synthetic modeling study. Geophysical Journal International, 766–783.

Crotwell, H. P., Owens, T. J., Ritsema, J., 1999. The TauP Toolkit : Flexible Seismic Travel-time and Ray-path Utilities. Seismological Research Letters 70 (April), 154–160.

Davies, D. R., Goes, S., Davies, J., Schuberth, B., Bunge, H.-P., Ritsema, J., nov 2012. Reconciling dynamic and seismic models of Earth's lower mantle: The dominant role of thermal heterogeneity. Earth and Planetary Science Letters 353-354, 253–269. URL https://www.sciencedirect.com/science/article/pii/S0012821X1200444X

Deng, J., Long, M. D., Creasy, N., Wagner, L., Beck, S., Zandt, G., Tavera, H., Minaya, E., 2017. Lowermost mantle anisotropy near the eastern edge of the Pacific LLSVP : constraints from SKS SKKS splitting intensity measurements. Geophysical Journal International 210 (June), 774–786.

Ford, H. A., Long, M. D., He, X., Lynner, C., 2015. Lowermost mantle flow at the eastern edge of the african large low shear velocity province. Earth and Planetary Science Letters 420, 12 – 22.

French, S. W., Romanowicz, B. A., 2014. Whole-mantle radially anisotropic shear velocity structure from spectral-element waveform tomography. Geophysical Journal International 199 (3).

Garnero, E. J., McNamara, A. K., Shim, S. H., 2016. Continent-sized anomalous zones with low seismic velocity at the base of Earth's mantle. Nature Geoscience 9 (7), 481–489.
URL http://dx.doi.org/10.1038/ngeo2733

Grund, M., Ritter, J. R. R., dec 2018. Widespread seismic anisotropy in Earth's lowermost mantle beneath the Atlantic and Siberia. Geology 47 (2), 123–126.
URL https://dx.doi.org/10.1130/G45514.1

Hall, S. A., Kendall, J. M., van der Baan, M., 2004. Some comments on the effects of lower-mantle anisotropy on SKS and SKKS phases. Physics of the Earth and Planetary Interiors 146 (3-4), 469–481.

Hernlund, J. W., Thomas, C., Tackley, P. J., 2005. A doubling of the post-perovskite phase boundary and structure of the earth's lowermost mantle. Nature 434 (7035), 882.

Kendall, J.-M., 2000. Seismic anisotropy in the boundary layers of the mantle. In: Karato, S., Forte, A., Liebermann, R., Masters, G., Stixtrude, L. (Eds.), Earth's Deep Interior: Mineral physics and Tomography From the Atomic to the Global Scale. Vol. 117 of Geophysical Monographs. American Geophysical Union, pp. 133–159.

Kendall, J.-M., Silver, P. G., 1998. Investigating causes of d" anisotropy. In: Gurnis, M., Wysession, M., Knittle, E., Buffet, B. A. (Eds.), The Core-Mantle Boundary Region. Vol. 28 of Geodynamics. American Geophysical Union, pp. 97–118.

Kennett, B. L. N., Engdahl, E. R., 1991. Traveltimes for global earthquake location and phase identification. Geophysical Journal International 105 (2), 429–465.
URL http://dx.doi.org/10.1111/j.1365-246X.1991.tb06724.x

Lay, T., Helmberger, D. V., 1983. A lower mantle S-wave triplication and the shear velocity structure of D". Geophysical Journal of the Royal Astronomical Society 75, 799–837.
URL http://dx.doi.org/10.1111/j.1365-246X.1983.tb05010.x

Lay, T., Young, C. J., 1991. Analysis of seismic sv waves in the core's penumbra. Geophysical Research Letters 18 (8), 1373–1376.

Long, M. D., 2009. Complex anisotropy in D beneath the eastern Pacific from SKS SKKS splitting discrepancies. Earth and Planetary Science Letters 283 (1-4), 181–189.
URL http://dx.doi.org/10.1016/j.epsl.2009.04.019

Long, M. D., Lynner, C., 2015. Seismic anisotropy in the lowermost mantle near the perm anomaly. Geophysical Research Letters 42 (17), 7073–7080, 2015GL065506.

Lynner, C., Long, M. D., 2014. Lowermost mantle anisotropy and deformation along the boundary of the african llsvp. Geophysical Research Letters 41 (10), 3447–3454, 2014GL059875.

Marquardt, H., Buchen, J., Mendez, A. S., Kurnosov, A., Wendt, M., Rothkirch, A., Pennicard, D., Liermann, H. P., 2018. Elastic Softening of (Mg 0.8 Fe 0.2)O Ferropericlase Across the Iron Spin Crossover Measured at Seismic Frequencies. Geophysical Research Letters 45 (14), 6862–6868.

Maupin, V., Garnero, E. J., Lay, T., Fouch, M. J., 2005. Azimuthal anisotropy in the d layer beneath the caribbean. Journal of Geophysical Research: Solid Earth 110 (B8). URL https://agupubs.onlinelibrary.wiley.com/doi/abs/10.1029/2004JB003506

Mcnamara, A. K., Van, P. E., Karato, S.-i., 2002. Development of anisotropic structure in the Earth's lower mantle by solid-state convection Is there evidence for the localization of dislocation creep in the lowermost mantle ? Nature 416 (March), 310–314.

Meade, C., Silver, P. G., Kaneshima, S., 1995. Laboratory and seismological observations of lower mantle isotropy. Geophysical Research Letters 22 (10), 1293–1296.

Moulik, P., Ekström, G., 2016. The relationships between large-scale variations in shear velocity, density, and compressional velocity in the earth's mantle. Journal of Geophysical Research: Solid Earth 121 (4), 2737–2771.

Murakami, M., Hirose, K., Kawamura, K., Sata, N., Ohishi, Y., 2004. Post-Perovskite Phase Transition in MgSiO3. Science 304 (5672), 855–858. URL http://www.sciencemag.org/cgi/doi/10.1126/science.1095932

Niu, F., Perez, A. M., 2004. Seismic anisotropy in the lower mantle: A comparison of waveform splitting of SKS and SKKS. Geophysical Research Letters 31 (24), 1–4.

Nowacki, A., Wookey, J., Kendall, J. M., 2010. Deformation of the lowermost mantle from seismic anisotropy. Nature 467 (7319), 1091–1094. URL http://dx.doi.org/10.1038/nature09507

Nowacki, A., Wookey, J., Kendall, J.-M., oct 2011. New advances in using seismic anisotropy, mineral physics and geodynamics to understand deformation in the lowermost mantle. Journal of Geodynamics 52 (3-4), 205–228. URL https://www.sciencedirect.com/science/article/pii/S0264370711000573

Pisconti, A., Thomas, C., Wookey, J., 2019. Discriminating Between Causes of D Anisotropy Using Reflections and Splitting Measurements for a Single Path. Journal of Geophysical Research: Solid Earth, 4811–4830.

Reiss, M. C., Long, M. D., Creasy, N., 2019. Lowermost Mantle Anisotropy Beneath Africa From Differential SKS SKKS ShearWave Splitting . Journal of Geophysical Research: Solid Earth, 1–25.

Restivo, A., Helffrich, G., 2006. Core—mantle boundary structure investigated using sks and skks polarization anomalies. Geophysical Journal International 165 (1), 288–302.

Richards, M. A., Lithgow-Bertelloni, C., 1998. The Dynamics of Cenozoic and Mesozoic Plate Motions. Reviews of Geophysics 36 (1), 27–78. URL http://www.agu.org/pubs/crossref/1998/97RG02282.shtml

Ritsema, J., Deuss, A., Heijst, H. J. V., Woodhouse, J. H., 2011. S40RTS: a degree-40 shear-velocity model for the mantle from new Rayleigh wave dispersion, teleseismic traveltime and normal-mode splitting function measurements. Geophysical Journal Internationalo 184, 1223–1236.

Romanowicz, B., Wenk, H.-R., 2017. Anisotropy in the deep earth. Physics of the Earth and Planetary Interiors 269, 58–90.

Savage, M., 1999. Seismic anisotropy and mantle deformation: What have we learned from shear wave splitting? Reviews of Geophysics 37 (1), 65–106.

Sidorin, I., Gurnis, M., Helmberger, D. V., 1999. Evidence for a Ubiquitous Seismic Discontinuity at the Base of the Mantle Evidence Seismic Base for of the a Ubiquitous at Mantle the. Science 286 (5443), 1326–1331.

Silver, P. G., 1996. Seismic Anisotropy beneath the continents: Probing the Depths of Geology. Annual Review of Earth and Planetary Sciences 24 (1), 385–432.

Silver, P. G., Chan, W. W., 1991. Shear wave splitting and subcontinental mantle deformation. Journal of Geophysical Research: Solid Earth 96 (B10), 16429–16454.

Silver, P. G., Long, M. D., 2011. The non-commutivity of shear wave splitting operators at low frequencies and implications for anisotropy tomography. Geophysical Journal International 184 (3), 1415–1427.

Silver, P. G., Savage, M. K., 1993. The Interpretation of shear-wave splitting parameters in the presence of two anisotropic layers. Geophysical Journal International 5 (January), 689–691.

Tateno, S., Hirose, K., Sata, N., Ohishi, Y., jan 2009. Determination of post-perovskite phase transition boundary up to 4400K and implications for thermal structure in D layer. Earth and Planetary Science Letters 277 (1-2), 130–136.
URL https://www.sciencedirect.com/science/article/pii/S0012821X08006687

Teanby, N. A., Kendall, J., Baan, M. V. D., 2004. Automation of Shear-Wave Splitting Measurements using Cluster Analysis. Bulletin of the Seismologial Society of America 94 (2), 453–463.

Thomas, C., Wookey, J., Simpson, M., 2007. D anisotropy beneath southeast asia. Geophysical Research Letters 34 (4).
URL https://agupubs.onlinelibrary.wiley.com/doi/abs/10.1029/2006GL028965

Tommasi, A., Mainprice, D., Canova, G., Chastel, Y., 2000. Viscoplastic self-consistent and equilibrium-based modeling of olivine lattice preferred orientations: Implications for the upper mantle seismic anisotropy. Journal of Geophysical Research: Solid Earth 105 (B4), 7893–7908.
URL https://agupubs.onlinelibrary.wiley.com/doi/abs/10.1029/1999JB900411

Vanacore, E., Niu, F., Feb 2011. Characterization of the d˝ beneath the galapagos islands using skks and sks waveform. Earthquake Science 24 (1), 87–99.
URL https://doi.org/10.1007/s11589-011-0772-8

Walker, A. M., Forte, A. M., Wookey, J., Nowacki, A., Kendall, J. M., 2011. Elastic anisotropy of D predicted from global models of mantle flow. Geochemistry, Geophysics, Geosystems 12 (10), 1–22.

Walpole, J., Wookey, J., Masters, G., Kendall, J. M., May 2014. A uniformly processed data set of SKS shear wave splitting measurements: A global investigation of upper mantle anisotropy beneath seismic stations. Geochemistry, Geophysics, Geosystems 15 (5), 1991–2010.

Walsh, E., Arnold, R., Savage, M. K., 2013. Silver and chan revisited. Journal of Geophysical Research: Solid Earth 118 (10), 5500–5515.

Wang, Y., Wen, L., 2007. Complex seismic anisotropy at the border of a very low velocity province at the base of the earth's mantle. Journal of Geophysical Research: Solid Earth 112 (B9), n/a–n/a, b09305.

Wessel, P., Smith, W. H. F., 1995. New version of the generic mapping tools. Eos, Transactions American Geophysical Union 76 (33), 329–329.
URL https://agupubs.onlinelibrary.wiley.com/doi/abs/10.1029/95EO00198

Wookey, J., Kendall, J.-M., 2007. Seismic anisotropy of post-perovskite and the lowermost mantle. In: Hirose, K., Brodholt, J., Lay, T., Yuen, D. (Eds.), Post-Perovskite: The Last Mantle Phase Transition. Vol. 174 of Geophysical Monograph. American Geophysical Union, pp. 171–189.

Wookey, J., Kendall, J.-M., oct 2008. Constraints on lowermost mantle mineralogy and fabric beneath Siberia from seismic anisotropy. Earth and Planetary Science Letters 275 (1-2), 32–42.
URL https://www.sciencedirect.com/science/article/pii/S0012821X08004883

Wookey, J., Kendall, J.-M., Rümpker, G., 2005a. Lowermost mantle anisotropy beneath the north pacific from differential s—scs splitting. Geophysical Journal International 161 (3), 829–838.

Wookey, J., Stackhouse, S., Kendall, J.-m., Brodholt, J., Price, G. D., 2005b. Efficacy of the post-perovskite phase as an explanation for lowermost-mantle seismic properties. Nature 438 (December), 1004–7.

Wuestefeld, A., Al-Harrasi, O., Verdon, J. P., Wookey, J., Kendall, J. M., 2010. A strategy for automated analysis of passive microseismic data to image seismic anisotropy and fracture characteristics. Geophysical Prospecting 58 (5), 755–773.

Wüstefeld, A., Bokelmann, G., 2007. Null detection in shear-wave splitting measurements. Bulletin of the Seismological Society of America 97 (4), 1204–1211.